Development of Ferroelectric Hafnium Oxide for Negative Capacitance Field Effect Transistors

Robin Athle
tna14rat@student.lu.se

Department of Electrical and Information Technology
Lund University

Supervisor: Mattias Borg

Co-Supervisor: Johannes Svensson

Examiner: Erik Lind

February 21, 2019

© 2019
Printed in Sweden
Tryckeriet i E-huset, Lund

Abstract

With the transistor being the workhorse in modern electronics it has been vastly improved since its invention. However, the previous go-to improvement method of scaling it down has reached a dead end. Power dissipation has become a large concern and is in need of a solution. In the pursuit of further improving the transistor structure and its performance new approaches are being evaluated. A very promising approach is the integration of ferroelectric materials enabling negative capacitance. With subthreshold slopes below 60 mV/decade demonstrated and hence enabling lower operation voltage a new era of transistor technology is protruding.

In this thesis a new recipe for deposition of hafnium oxide thin films using plasma enhanced atomic layer deposition has been developed. Thin hafnium oxide films have been fabricated, characterized and their properties optimized. The films are embedded into a titanium nitride metal-insulator-metal (MIM) structure for electrical characterization. With the use of Poole-Frenkel, Schottky and Fowler-Nordheim models the leakage current mechanisms of the thin films have been evaluated.

For the first time, observation of the ferroelectric characteristics in undoped hafnium oxide thin films grown using plasma enhanced atomic layer deposition are reported. The presence of ferroelectricity was confirmed with polarization measurements, with values of the remanent polarization P_r up to $8.75\mu C/cm^2$ for a 10nm thick film with a dielectric constant ϵ_r up to 30.

Popular Science Summary

Du vaknar på morgonen kollar på din mobiltelefon om det hänt något nytt och spännande, tar datorn med dig till jobbet eller plugget och efter en lång dag sätter du dig i soffan och slår på Tvn. Alla dessa prylar har en central roll i vår vardag och är baserade på en gemensam nämnare som möjliggjort detta– transistorn. I din mobiltelefon finns det ungefär 200 miljarder av dem, i datorn ännu fler. Transistorn är en av de största uppfinningarna i modern tid och har skapat den digitala värld vi nu kan uppleva. Så vad är en transistor och hur fungerar den? En transistor kan liknas vid strömbrytare som antingen kan vara påslagen och släpper då igenom ström eller avslagen och blockerar då att ström flödar. Den består av tre stycken terminaler som är benämnda Gate, Source och Drain. Dessa är kopplade på ett sätt så att om en spänning läggs över gaten ändras motståndet mellan source och drain vilket öppnar en kanal där elektroner kan färdas. Detta är vad som ger upphov till "på"-läget där ström kan flöda genom strukturen.

Den konventionella transistorn tillverkades av grundämnet kisel som är billigt och lätt att jobba med och har fungerat fantastiskt för ändamålet under många år. De prestandaförbättringar som skett för transistorn kan till allra största grad tillägnas nedskalningen av strukturen. Det har sänkt energiförbrukningen, minskat materialåtgången och möjliggjort integration av miljardvis transistorer på mindre chip. Tyvärr har fortsatt nedskalning av kiseltransistorn avstannat då vi har nått den fysikaliska gränsen för kisel. Ett problem som uppstått är att det genereras väldigt mycket värme när transistorn slås av och på. Värme som inte kan ledas bort på ett enkelt sätt. Detta skapar betydande energiförluster vilket är ett stort problem. För att lösa detta problem behöver transistorns drivspänning dvs den spänning som krävs för att slå på transistorn, minska. Svårigheterna i detta är att man måste bibehålla mängden ström samtidigt som man minskar spänningen något som visat sig vara utmanande.

En lösning på problemet är att implementera vad man kallar för ferroelektriska material i transistorstrukturen. Ett ferroelektriskt material har nämligen egenskapen att man kan ändra dess spontana uppladdning genom att lägga på ett elektriskt fält. Denna egenskap möjliggör att man kan sänka drivspänningen samtidigt som man för låga spänningar behåller samma strömnivåer.

I detta examensarbete har jag tillverkat tunna filmer av hafnium oxid med målet av visa på materialets ferroelektriska egenskaper.

Acknowledgements

I wish to give a special thanks to my supervisor assistant professor Mattias Borg for granting me the opportunity of this thesis along with his insight and continuous guidance.

A warm thanks to Dr. Karl-Magnus Persson for all the ours spent teaching me the equipment in the lab.

I would like to thank Anton Persson for our collaboration on the subject of ferroelectrics and the many intriguing discussions we have had leading to improvements and results.

A big thanks to the LNL staff making research of this caliber possible.

Finally I would like to express my gratitude to my family who have supported my studies and given guidance when in need. I would like to give some extra credit to my father Ronny Athle who has been pushing me to always strive for improvement as well as my sister Isabelle who has been a role model and inspiration for me through my studies.

"All men are created equal. Some work harder in preseason."
- Emmitt Smith

Abbreviations

AFM Atomic Force Microscopy. 24

Al Aluminum. 10

Al_2O_3 Aluminim Oxide. 20

ALD Atomic Layer Deposition. 20

Au Gold. 29

$BaTiO_3$ Barium Titanate. 6

BOE Buffered Oxide Etch. 27

CH_3 Methyl. 20

CMOS Complementary Metal Oxide Semiconductor. 9

CO Carbon monoxide. 20

CO_2 Carbon dioxide. 20

CVD Chemical Vapor Deposition. 20

DC Direct Current. 12

eV Electron Volt. 3

FeFET Ferroelectric Field Effect Transistor. 6

FeRAM Ferroelectric Random Access Memory. 6

GIXRD Grazing incidence X-Ray Diffraction. 10

GPC Growth per Cycle. 32

HfO_2 Hafnium dioxide. 1

IC Integrated Circuit. 6

LNL Lund Nano Lab. 21

MOSFET Metal Oxide Semiconductor Field Effect Transistor. 1

MSE Mean Square Error. 24

O Oxygen. 20

P-E Polarization-Electric field. 7

$PbTiO_3$ Lead Titanate. 6

Si Silicon. 1

SiO_2 Silicon dioxide. 9

$SrBi_2Ta_2O_9$ Strontium Bismuth Tantalite. 6

SS Subthreshold Slope. 1

TEMAHf Tetrakis(ethylmethylamido)hafnium(IV). 21, 31

Y Yttrium. 10

List of Symbols

Term	Description	Units/Value
P_r	Remanent polarization	$\mu C/cm^2$
P_s	Spontaneous polarization	$\mu C/cm^2$
E_c	Coercive field	kV/cm^2
E_g	Band gap energy	eV
ϵ_r	Relative permittivity	
ϵ_0	Vacuum permittivity	$8.854 * 10^{-14} F/cm^2$
E_k	Electric Field of material k	kV/cm
C_k	Capacitance per area of material k	F/cm^2
Q	Surface charges per area	C/cm^2
Ψ_s	Surface potential	V
V	Voltage	V
t	thickness	cm
V_g	Gate voltage	V
V_c	Coercive Voltage	V
k	Boltzmann's constant	$8.617 * 10^{-5} eV/K$
T	Temperature	K
q	Elementary charge	$1.602 * 10^{-19} C$
N_A	Acceptor concentration	C/cm^2
C_{gd}	Gate Drain Capacitance	F

Term	Description	Units/Value
C_{gg}	Gate Capacitance	F
C_{gs}	Gate Source Capacitance	F
C_{sd}	Source Drain Capacitance	F
C_{ox}	Oxide Capacitance	F
SS	Subthreshold Slope	$mV/decade$
R	Resistance	Ω
ρ	Resistivity	Ωm
V_{ds}	Drain Source Voltage	V
V_{gs}	Gate Source Voltage	V
d	Distance between capacitor plates	nm
U	Energy	$a.u.$
A	Area of plates	m^2
Θ	Angle	$Degrees$
Δ	Phase shift	$Degrees$
Ψ	Amplitude ratio	
I	Current	A

Table of Contents

1 Introduction **1**

2 Field Effect Transistor and Ferroelectrics **3**
- 2.1 Background . . . 3
- 2.2 The MOSFET Structure & Operation . . . 3
- 2.3 Ferroelectricity . . . 5
- 2.4 Ferroelectric Hafnium Oxide . . . 9
- 2.5 Negative Capacitance . . . 12
- 2.6 MIM Cap Energy Band Theory & Leakage Mechanisms . . . 15
- 2.7 Processing & Characterization Methods . . . 20

3 Fabrication & Calibration **27**
- 3.1 Sample Fabrication Process . . . 27
- 3.2 TEMAHf Calibration . . . 31

4 Electrical Characterization Method **35**
- 4.1 Leakage Current . . . 35
- 4.2 Polarization-Electric field Measurement . . . 35

5 Results & Analysis **39**
- 5.1 TEMAHf Calibration in Fiji F200 . . . 39
- 5.2 Sample Series Specifications & Electrical Characterization . . . 41
- 5.3 Effective Potential Barrier Height . . . 55
- 5.4 Atomic Force Microscopy . . . 59
- 5.5 P-E Measurements . . . 60

6 Conclusions **65**

References **67**

A MATLAB Code For P-E Curves **73**

B Old Recipe HfO2 **75**

List of Figures

2.1 Schematic of an n-type MOSFET. 4
2.2 Arrangement of the 32 crystal classes. 5
2.3 First hysteresis curve of a ferroelectric material [1]. 6
2.4 **1** Energy landscape U of a ferroelectric material in the absence of an electric field. **2** Landscape change in presence of an electric field smaller than the coercive field E_c. **3** Evolution of energy landscape when an electric field greater than E_c is applied and the polarization passes trough the state of negative capacitance. 7
2.5 Domains with spontaneous polarization with and without the presence of an electric field. 8
2.6 Ferroelectric P-E hysteresis loop. The hexagons with gray and white regions represent schematically repartition of two polarization states in the material at different fields [2]. 8
2.7 Binary diagram of Hf-O [3]. 10
2.8 P-V and C-V hysteresis curves for a thickness series of pure HfO_2 thin films crystallized in the precence of a PVD-TiN top electrode (left). TEM micrograph comparison of the 6nm and 20nm HfO_2 films [4]. . 11
2.9 (a) GIXRD data for a thickness series of pure HfO_2 crystallized in the presence of a PVD-TiN top electrode. The inset shows an enlargement of the prominent reflexes for the monoclinic, orthorhombic and cubic phase structure, which were used for the calculation of the monoclinic phase fraction. (b) Calculated monoclinic phase fraction and corresponding values of remanent polarization P_r as a function of film thickness. [4]. 12
2.10 Grazing incidence x-ray diffraction measurements of two Si:HfO2 samples of the same composition where crystallization was induced with and without capping. [5]. 13
2.11 Schematic of a parallel plate capacitor with polarization of the dielectric, where Q denotes the charge and d the plate separation. 14
2.12 P-E curve of a ideal capacitor. 14
2.13 Hysteresis of a ferroelectric material. 14

2.14 Schematic of Hysteresis curve for a ferroelectric material where the red curve denoted the measured, turquoise the accurate polarization where the negative differential capacitance is present in the barrier region. 15
2.15 Schematic of energy band structure of MIM structure. 16
2.16 Tunneling mechanisms of insulators schematically displayed. Image taken from [6]. 19
2.17 A schematic view of the ALD process for depositing Al_2O_3. (1) initiation of process, adding first precursor (TMA). (2) one TMA reacting with the surface oxide releasing CH3. (3) The excess TMA and methane are removed using a carrier gas or protrusion step. (4) A oxygen plasma pulse reacts with the surface. (5) One atomic layer Al_2O_3 deposited. Image modified from [7]. 21
2.18 A schematic view of the evaporation chamber utilizing a shadow mask. 22
2.19 Different polarizations of light. ***A*** Linear, ***B*** Circular and ***C*** Elliptical. Image taken from https://www.jawoollam.com. 23
2.20 Schematic of experimental setup for ellipsometry measurements. . . . 23
2.21 Schematic of experimental setup for an atomic force microscope. . . 25

3.1 Schematic of the sample after etching of SiO_2. 27
3.2 Schematic of the sample after TiN BE sputtering. 28
3.3 Schematic of the sample after HfO_2 deposition. 28
3.4 Schematic of the sample after top layer capping with TiN. 29
3.5 Schematic of the sample after evaporation. 30
3.6 Optical spectroscopy image of fabricated sample after metal deposition. 30
3.7 Schematic of the sample after TiN etching. 31
3.8 Schematic of the entire sample process step by step. 31
3.9 Sample placing on the chuck of the ALD. 32

4.1 Measurement setup for P-E. 36

5.1 Calibration of GPC for TEMAHf source in Fiji F200 ALD. 40
5.2 Calibration of GPC for TEMAHf source in Fiji F200 ALD. 41
5.3 I-V characteristics for sample series 3 of different device area. 4nm HfO_2 deposited with varying plasma pulse duration. 43
5.4 Leakage current at 1V and breakdown voltage for xsmall structure of 4nm thin HfO_2 with increasing plasma duration. 44
5.5 Impact on I-V characteristics, leakage current at 1V and breakdown voltage for xsmall structure of 4nm thin HfO_2 due to increasing plasma power. 45
5.6 Impact on J-V characteristics, leakage current at 1V and breakdown voltage for xsmall structure of 8nm thin HfO_2 with respect to varying deposition temperatures. 47
5.7 Impact on J-V characteristics, leakage current at 1V and breakdown voltage for xsmall structure of 4nm thin HfO_2 with respect to varying oxygen flow. 49

5.8 Impact on J-V characteristics, leakage current at 1V and breakdown voltage for xsmall structure of 4nm thin HfO_2 with respect to varying plasma purge duration. 51
5.9 I-V characteristics, leakage current at 1V and breakdown voltage for xsmall structure of 10nm thin HfO_2 with optimized growth conditions. 53
5.10 (a) Current density, (b) FN, (c) PF and (d) Scottky plots of plasma duration series. 55
5.11 (a) Current density, (b) FN, (c) PF and (d) Schottky plots of optimized sample as deposited and post annealing. 57
5.12 2D and 3D AFM images of HfO_2 of the optimized sample for small and large areas. 60
5.13 (A-C) V-T, (D-F) P-E and (G-I) ϵ_r-E curves of three different devices from the optimized sample with an area of $\sim$1.4e-5 cm^2 61
5.14 I-T curves of ferroelectric oxides by Karine Florent. Image Taken from [8] 63

A.1 MATALB code for P-E curves. 73
A.2 MATALB code for P-E curves. 74
A.3 MATLAB code to read input data from measurements. 74

B.1 Standard recipe for HfO_2 at 200°C. 75

List of Tables

5.1 Deposition conditions of sample series 1. 42
5.2 Deposition conditions of sample series 2. 44
5.3 Deposition conditions of sample series 4. 46
5.4 Deposition conditions of sample series 4. 48
5.5 Deposition conditions of sample series 5. 50
5.6 Deposition conditions of optimized sample ("series 6"). 52
5.7 Summary of results from analysis of the J-V characteristics using FN, SE and PF models. 59
5.8 Summary of metrics derived from P-E measurements. 62

Chapter 1 Introduction

Cellphones, tablets and computers are just a few applications that are based on one crucial and fundamental structure – the transistor. The Metal Oxide Semiconductor Field Effect Transistor (MOSFET) has provided exceptional improvements in computational power since its invention in 1959 at Bell Labs [9]. The conventional MOSFET has been fabricated out of Silicon (Si) since the beginning, primarily due to its low cost. The development of the transistor structure has been focused on scaling it down to smaller dimensions. The reason for this is simply since it improves the speed of data transfer and reduces the material consumption at manufacturing. The scaling of the MOSFET has been very successful down to the nanometer scale and has provided huge performance increases. However, scaling the transistor beyond todays dimensions has proven to be very difficult. Scaling has reached a dead end where further scaling does not yield performance improvements. The reason for this is due to physical limitations of Silicon as a material as well as limitations in the gate oxide thickness. In order to keep improving the transistor new research is being conducted in various fields with the hope of finding a solution.

One promising approach to keep improving the characteristics of the transistor is to implement so called ferroelectric materials to a generate negative capacitance. The use of ferroelectrics in transistors can improve the switching speed for low power applications [10]. However the main benefit of integrating ferroelectrics in transistors is that they have the ability to lower the Subthreshold Slope (SS) < 60mV/decade which in return enables a decrease in the transistor operation voltage thus decreasing the power consumption [11].

In today's transistors the use of Hafnium dioxide (HfO_2) as gate oxide is very popular due to its "high-k" value (high permittivity). Recently it has also been shown that undoped HfO_2 exhibits ferroelectric behaviour provided certain fabrication conditions are met [4]. Since hafnium oxide is currently used as gate oxide the change in fabrication process required to implement ferroelectric hafnium oxide is small. This makes it very attractive and promising.

In this thesis the main objective is to deposit, characterize and improve the quality of hafnium oxide films and evaluate their dielectric and leakage properties via electrical and optical measurements. Ferroelectricity of the films will also be investigated in crystallized undoped hafnia films.

Chapter 2

Field Effect Transistor and Ferroelectrics

2.1 Background

The development of microelectronics has during the last several decades enabled portable electronic devices such as smartphones and watches, tablets and laptops. These are devices used on a day-to-day basis for most of us. Not only are these gadgets widely available but they are also improving every year. This can be attributed to the discovery of new technologies. Every year products launched have been faster, smaller and less power consuming. This development requires enormous amounts of research and finance, granting millions of people employment all thanks to the invention of the transistor in 1926 by Julius Edgar Lilienfeld. The development has come a long way since 1926 with many astonishing breakthroughs. Yet there may be a lot more to come.

2.2 The MOSFET Structure & Operation

The MOSFET has revolutionized the industry with its high performance and low cost. The conventional MOSFET is based on silicon, a group IV element, and belongs to a special type of materials - the semiconductors. This means that silicon at room temperature has a band gap. This band gap is in the range of 1.14 Electron Volt (eV). [12]. The MOSFET is a so called "three-terminal" device which means it has three terminals (three contacts). These are denoted Gate, Source and Drain. These terminals are where voltage is applied to the transistor. Generally there are two different types of MOSFETs, p-type and n-type. The difference between the two types depends on the doping of the substrate. The most common is the n-type MOSFET which is depicted in figure 2.1.

The n-type MOSFET has a p-doped semiconductor substrate as well as two smaller regions with heavy n-doping (denoted n+). If this instead was a p-type MOSFET the substrate would be n-doped and the two smaller regions heavily p-doped. From figure 2.1 one can see the gate oxide separating the gate metal from the substrate. This oxide has a crucial purpose since it has insulating properties which inhibits leakage. The purpose of the oxide is to hinder the charge in the channel from reaching the gate metal. Why this is so important can be understood by studying the operation of a MOSFET. It uses an electric field which is generated once a bias is applied to the gate terminal. The applied bias to the gate electrode

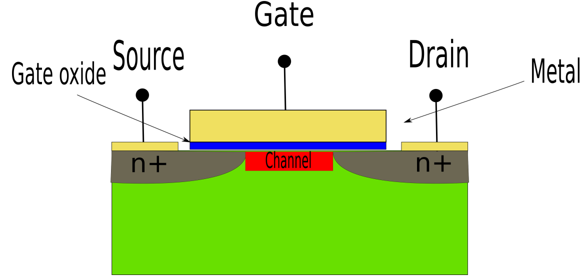

Figure 2.1: Schematic of an n-type MOSFET.

controls the conductivity of the channel. When a bias is applied at the gate a reduction of the built-in energy barrier occurs. This can lead to inversion of the p-type substrate close to the gate enabling electrons to flow from the source to the drain.

As mentioned earlier, scaling has been the main improvement driver to the MOSFET since it was invented, however this approach is no longer viable due to several reasons. Scaling down the gate length further will introduce short-channel effects [13] which degrades the performance. There is also a physical limitation of the insulating gate oxide where scaling it down will give rise to leakage currents. Moreover the heat generation during the switching process along with the inability to remove this heat leads to large thermal challenges in the form of power dissipation [14].

One way to significantly lower the power dissipation per switching event is to reduce the operation voltage of the transistors. Since the power scales with the operation voltage squared ($P \propto V_{DS}^2$), huge power reductions are possible. One of the primary factors limiting the operating voltage of a transistor is the so called "subthreshold swing" SS, which represents the inverse of the change of current that can be obtained for a unit change in gate voltage. The SS is defined in equation 2.1 and has two dependencies where the first one relates the change in surface potential in the channel to the change in current and is, at room temperature, limited to 60 mV/decade (n-factor in equation 2.1) [14]. However the second term called the "body factor", m, is based on a capacitive voltage divider between the gate voltage Vg and the surface potential Ψ_s.

$$SS = \left(\frac{dlogI_D}{dV_G}\right)^{-1} = \left[\left(\frac{d\Psi_s}{dV_G}\right)\left(\frac{dlogI_D}{d\Psi_s}\right)\right]^{-1} = n \cdot m \tag{2.1}$$

where

$$m = \frac{dV_G}{d\Psi_s} = 1 + \frac{C_s}{C_0} \tag{2.2}$$

and

$$n = \frac{2.3k_BT}{q} \tag{2.3}$$

Generally the m-term term always exceeds one and at best approaches one when a very high-k insulator is used. By introducing a negative capacitance in series with the conventional insulator it is possible to reduce the second term to

less than one which lowers the SS to below 60mV/decade. This improvement in SS enables a lower operating voltage of below 0.5V while still providing sufficiently high current [11], [14], [15]. This makes a great case for negative capacitance FETs (NCFETs), ferroelectric memories and ferroelectric gate oxides which are attractive for low power applications.

2.3 Ferroelectricity

2.3.1 Polarization & Crystal Classes

In order to understand ferroelectricity one must know about polarization. One purpose of a dielectric is to function as an insulator blocking charge to pass through it. However when an external electric field is applied, polarization of the dielectric can occur. This arises from changing the equilibrium positions of the charges in the dielectric. From this positional change of charges very special properties arise. These are classified in the following order: piezoelectricity, pyroelectricity and ferroelectricity [8]. These features are dependent on the crystalline nature of the materials and will be described below.

In regards to crystalline materials they are classified into 32 crystal classes [8] which are schematically displayed in figure 2.2.

When polarization arises from mechanical strain this is known as piezoelectricity. This happens when there's a change in the shape of the crystal and negative charges separate from positive ones at each crystal unit cell [8]. This gives rise to a dipole moment which is known as piezoelectricity. In order for the piezoelectric effect to occur it was established that the crystal has to be non-centre-symmetrical, a criteria 21 of the 32 classes fulfills. Nevertheless there is one class out of these 21 that still does not yield a dipole moment. Out of the remaining 20 classes 10 of them have a spontaneous polarization that is dependent on temperature. These are known as pyroelectrics. Lastly if the pyroelectric crystal's spontaneous polarization can be reversed by applying an electric field it is further classified as ferroelectric [16].

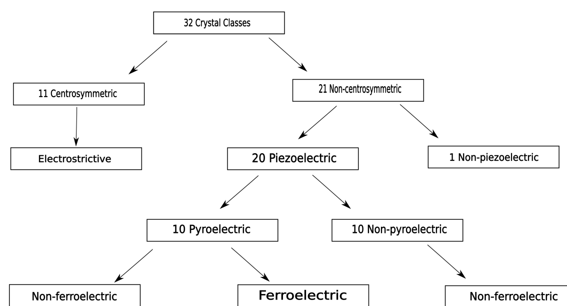

Figure 2.2: Arrangement of the 32 crystal classes.

2.3.2 Ferroelectricity & Its Properties

The first paper presenting ferroelectricity dates back all the way to 1920 when Joseph Valasek presented *Piezoelectric and allied phenomena in Rochelle salt* [1]. He stated in the paper that *"permanent polarization is the natural state"* of Rochelle salt and he presented the first ever hysteresis curve of a ferroelectric material (see figure 2.3). This sparked the evolution of ferroelectric materials and various research was conducted with the main purpose of finding more ferroelectric materials. However the interest in ferroelectrics picked up new steam during the beginning of the second World War in 1939. The interest was to use ferroelectrics in sonar systems to detect submarines [17]. Between 1942-1944 the first perovskite ferroelectric was discovered - Barium Titanate ($BaTiO_3$). A ceramic compound with a dielectric constant exceeding 1000. The discovery of barium titanate had a huge impact on the science of ferroelectric materials since it demonstrated the ferroelectric property in regular oxide materials.

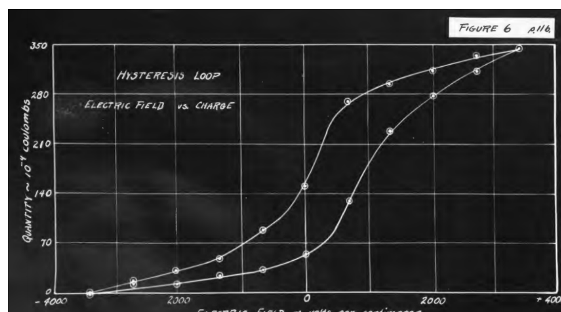

Figure 2.3: First hysteresis curve of a ferroelectric material [1].

Along with Barium Titanate, Lead Titanate ($PbTiO_3$) and other ceramics such as Strontium Bismuth Tantalite ($SrBi_2Ta_2O_9$) have been widely researched. These perovskite materials possess ferroelectric properties in their bulk form which have made them of great interest in the field. However there are pressing issues when trying to incorporate them into Integrated Circuit (IC) processing. First and foremost at thin film thickness the perovskites' ferroelectric behaviour becomes very unstable. Secondly they have proven to be incompatible with the standardized IC processing when scaled down beyond the 130 nm node [8].

The reason ferroelectric materials are so attractive are due to the unique property, of being able to possess two polarizations. A property which makes them very attractive for memory applications. Ferroelectric Random Access Memory (FeRAM) as well as Ferroelectric Field Effect Transistor (FeFET) have been developed [8]. In a digital circuit the two separate polarization states at equilibrium denote the logic states "one" and "zero". The explanation to this lies in thermodynamics. For these structures there are two (equally) thermodynamically stable configurations that corresponds to an energy minimum. These have equivalent but opposite polarization. The polarization at zero electric field is known as the remanent polarization P_r and has the unit $[\mu C/cm^2]$. The two states are separated by a potential barrier and both are equally energetically favoured over the non-

polar configuration [18]. The polarization can be reversed in the presence of an electric field since this lowers the potential barrier between the states and enables the central ion of the unit cell to change position. This is schematically visualized in figure 2.4.

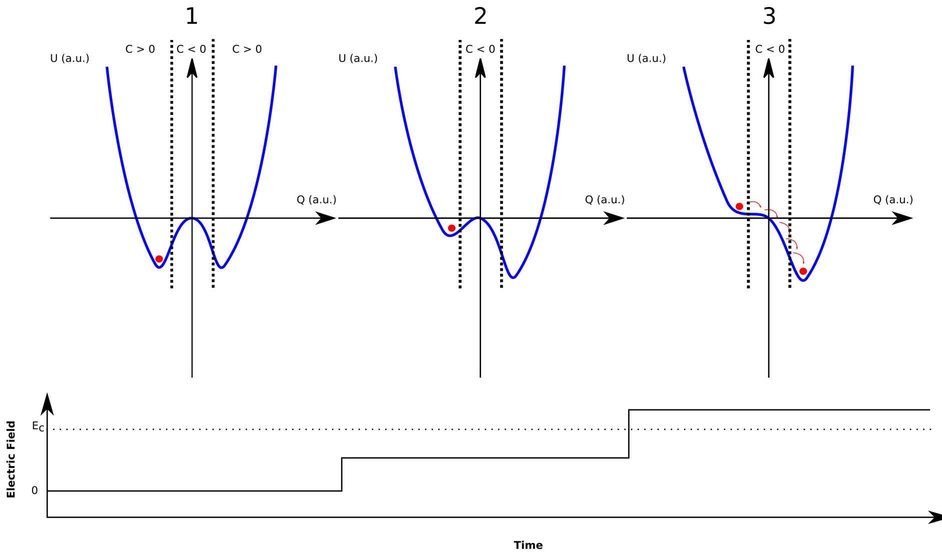

Figure 2.4: 1 Energy landscape U of a ferroelectric material in the absence of an electric field. **2** Landscape change in presence of an electric field smaller than the coercive field E_c. **3** Evolution of energy landscape when an electric field greater than E_c is applied and the polarization passes trough the state of negative capacitance.

In order to understand the hysteresis curve of a ferroelectric material one must note that a ferroelectric material does not have a uniform polarization but is instead divided into domains with different polarization directions. If the spontaneous polarization direction of each domain is completely random or distributed in a way so that no macroscopic polarization occurs the material will not have a remanent polarization. In figure 2.5 the influence of an electric field on the domains is displayed. Between domains there are domain walls present which have varying thickness. In these walls the polarization changes repeatedly and rapidly between domain polarization's [2]. These domains can arise from different factors such as uniformly oriented spontaneous polarization in a small local area or electrical and thermal treatment of the sample.

When the domains are in the presence of an external electric field the dipole moments rotate in order to align themselves with the applied field. When the electric field is removed there is still a polarization present. This polarization is the remanent polarization P_r mentioned earlier. This is a unique property of ferroelectric materials. The precence of an electric field changes the domain walls and can even eliminate them, this can be seen in the Polarization-Electric field (P-E) measurement and hysteresis curve which is a consequence of domain wall

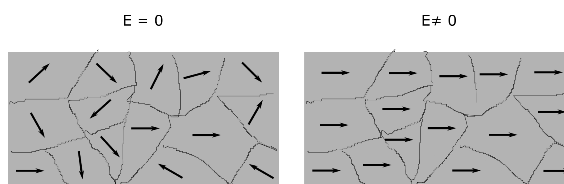

Figure 2.5: Domains with spontaneous polarization with and without the presence of an electric field.

switching. [2].

This following paragraph explains the appearance of a general hysteresis loop see figure 2.6. Please note that this explanation is taken from *Dragan Damjanovic - The Science of Hysteresis, Chapter 4* reference [2].

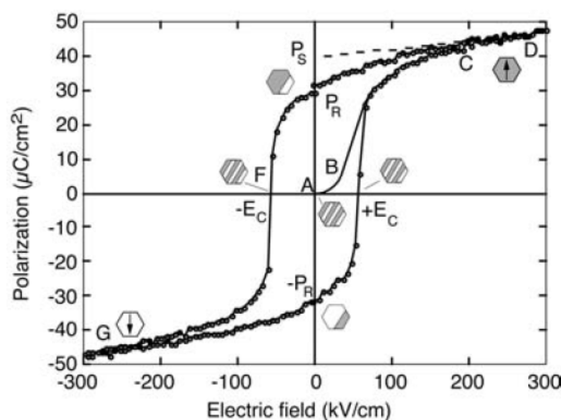

Figure 2.6: Ferroelectric P-E hysteresis loop. The hexagons with gray and white regions represent schematically repartition of two polarization states in the material at different fields [2].

At small values of the applied electric field the polarization increases linearly along with the amplitude of the field. This can be seen in segment AB in figure 2.6. In this region the field is not strong enough to switch domains with unfavorable polarization direction. However as the field increases the domains will start to switch along the direction of the applied electric field (BC). It is important to note that some domains cannot switch fully to the direction of the field due to physical constraints. Nevertheless these domains still change in the direction of the field to their fullest ability. The polarization is now firmly nonlinear. This proceeds until all domains are aligned (point C) and a linear behaviour is observed (CD). As the field is weakened some domains will switch back. However at zero field the polarization is nonzero. This polarization is the remanent polarization P_r mentioned previously. In order to remove the polarization a reverse field has to be applied (point F). This will cause a new alignment of the domains and as the negative field is increased a saturation point will be reached (point G). By

then reducing the field to zero and reversing it the cycle of the hysteresis loop is completed. The field necessary to bring the polarization back to zero is denoted the coercive field E_c. Furthermore the value of the coercive field is not an absolute threshold field and that if a low electric field is applied over a long time the polarization will still, sooner or later, switch [2]. Lastly one must understand that the absolute value of the polarization cannot be measured only the change of it can.

2.4 Ferroelectric Hafnium Oxide

As mentioned previously there has been a vast interest in ferroelectrics for a long time and research has mainly been focused on perovskite structures such as Barium Titanate, Lead Titanate and Strontium Bismuth Tantalite. However these structures have been found challenging to integrate with IC processing since they have a small bandgap, requires large thickness in order to retain stable ferroelectric behaviour and not to mention exhibit poor compatibility with Silicon technology [8]. One promising substitute to the perovskite structures is hafnium dioxide HfO_2 also known as "hafnia".

Hafnia has been of interest to scientists for a long time, research dates back to as early as the mid-19th century where hafnia and zirconia were studied for their ceramic properties. However it is of the last decade where they have been rediscovered for Complementary Metal Oxide Semiconductor (CMOS) application and fabrication due to their high dielectric constant of up-to $\sim$ 70 compared to Silicons 3.9 [4]. During both these periods the main interest was to investigate and gain knowledge about the polymorphism of the oxide. In hafnia for the bulk system four different crystal phases are known [4]. The monoclinic, the tetragonal the cubic and the orthorombic phase can at different temperatures and pressures be observed. However for CMOS-compatible thin films of Hafnia there are many more factors influencing the crystalline phase stability. It has been shown that doping [19] [20], growth temperatures [21, 22], surface energy effects, strain by grain size and film thickness [4] as well as thermal treatments [23,24] and deposition methodology impacts the outcome. The binary diagram under 1 atm of Hafnium and Oxygen is displayed in figure 2.7. In the binary phase diagram the three phases are shown. However notable is that at high pressure orthorhombic structures can be observed. OI and OII phases can be obtained at pressures between 4 to 16GPa [25].

According to the literature [26] the highest dielectric constant of Hafnia possible is around 70 and comes from the tetragonal phase. This compared to Silicon dioxide (SiO_2) with 3.9 is extremely high and attractive for IC fabrication. It has also been shown that doping the oxide with e.g Silicon stabilizes the tetragonal phase and therefore has higher dielectric constant than undoped Hafnia [27]. The use of a TiN capping layer has also been shown by *Polakowski et al* in 2015 to avoid premature crystallization of the HfO_2 which suppresses the monoclinic phase. *Boescke* et al [5] showed in 2011 ferroelectric films of HfO_2 with an orthorombic phase believed to be $Pbc2_1$. It is this phase that's believed to induce the ferroelectric behaviour in the thin film. Along with encapsulation using TiN

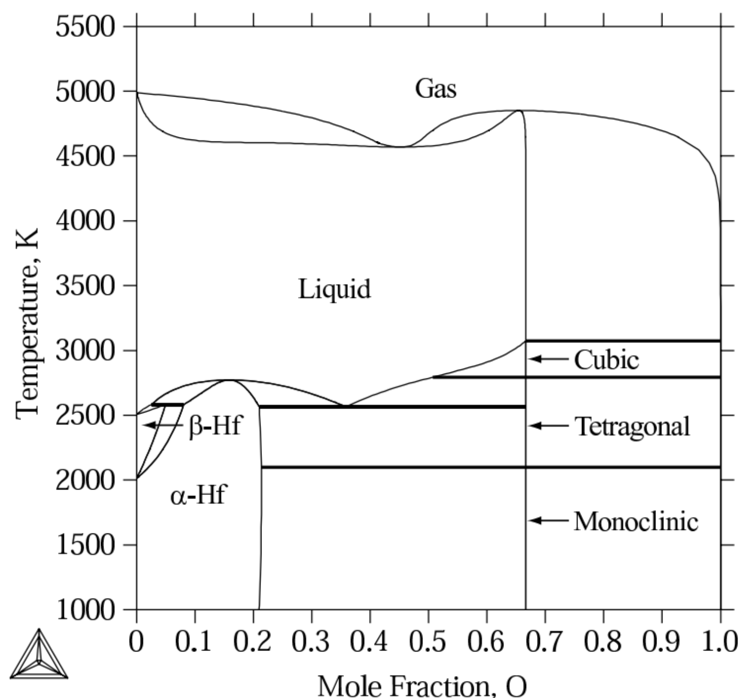

Figure 2.7: Binary diagram of Hf-O [3].

it has been shown to suppress the monoclinic phase and give the more desired, high-k tetragonal and cubic phase. There have previously been several studies conducted where dopants have been introduced in the oxide to stabilize these phases and generate the ferroelectric properties. Aluminum (Al) [28], Yttrium (Y) [29], Lanthanum [30] [31] and Silicon (Si) [5] [32] have been used to successfully show ferroelectric behaviour in hafnium oxide. There is a lot less research concerning ferroelectricity in undoped HfO_2, making this a more appealing field. The appearance of ferroelectricity in pure HfO_2 is argued to be intrinsic in nature [4] which makes it an even more interesting subject. *Polakowski* et al [4] studied how the thickness of the HfO_2 thin film impacted the ferroelectricity. Ferroelectricity was found in the ranges of 6-12nm thin films. In figure 2.8 clear hysteresis curves are presented where the dependence on thin film thickness is presented. Where the strongest hysteresis is achieved for the 6 and 8nm thin films. Figure 2.8 also shows how grain size impacts the ferroelectric behaviour. The use of Grazing incidence X-Ray Diffraction (GIXRD) analysis shows a clear suppression of the monoclinic phase, see figure 2.9. The main focus of this thesis will in regard to the above motivation primarily be based on ferroelectric behaviour in undoped HfO_2.

2.4.1 Capping Using Titanium Nitride

Capping the dielectric with electrodes of titanium nitride has been seen to suppress the monoclinic phase of HfO_2 and is regarded as an important step to make the

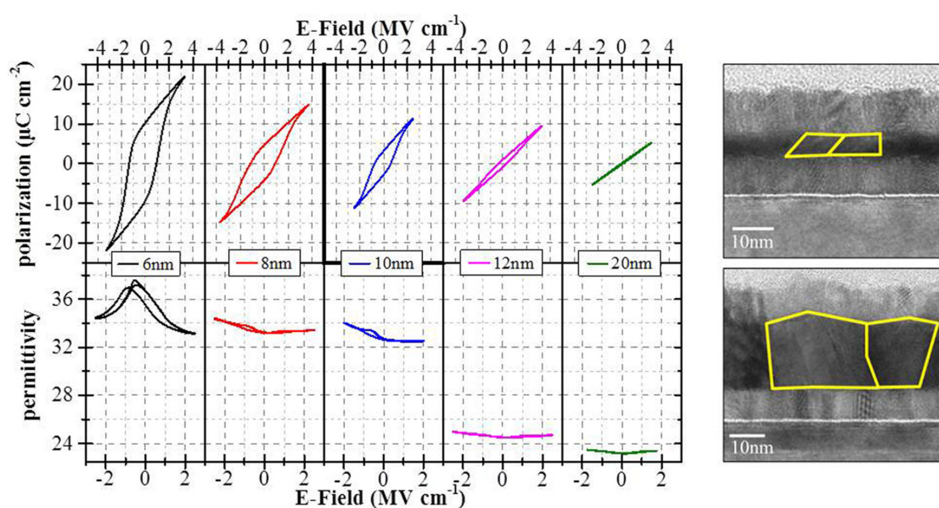

Figure 2.8: P-V and C-V hysteresis curves for a thickness series of pure HfO_2 thin films crystallized in the precence of a PVD-TiN top electrode (left). TEM micrograph comparison of the 6nm and 20nm HfO_2 films [4].

oxide ferroelectric. This section will be devoted to the purpose of capping and the use of titanium nitride.

TiN capping during high temperature annealing plays an important role in improving the properties of dielectric films. Ferroelectric hafnia has been sandwiched between top and bottom electrodes made out of TiN [4, 33, 34]. Triysos et al showed in 2006 the correlation between suppression of the monoclinic phase in HfO_2 and capping using TiN [34]. They achieved a mixture of monoclinic and tetragonal HfO_2 in room temperature instead of a fully monoclinic HfO_2, which was observed without the TiN capping layer. Their explanation for this phenomena was that the volume expansion resulting from the annealing process is limited owing to mechanical constraints imposed by the capping layer. They also found that the use of a TiN capping layer during the annealing process reduces the void formations in the film since the capping layer constrains the planarity of the top surface. Finally surface roughness was also improved.

Böscke et al found similar dependencies in 2011 for Si-doped HfO_2 thin films [5] [35]. They argue that the use of capping for Si-doped hafnia inhibits the monoclinic phase and instead gives rise to the ferroelectric orthorombic phase belonging to the space group $Pbc2_1$. Their results using GIXRD measurements showed basically no m-peaks after crystallization when using a TiN capping layer, see figure 2.10.

To summarize, it is generally believed that the use of a TiN capping layer improves the ferroelectric features of HfO_2-based thin films. The most promising and applicable structure seems to be the sandwich formation where the thin film is surrounded by TiN as top and bottom electrode [36].

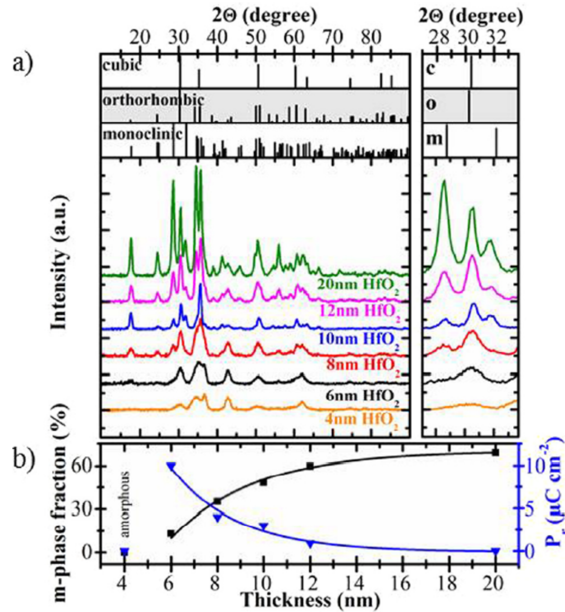

Figure 2.9: (a) GIXRD data for a thickness series of pure HfO_2 crystallized in the presence of a PVD-TiN top electrode. The inset shows an enlargement of the prominent reflexes for the monoclinic, orthorhombic and cubic phase structure, which were used for the calculation of the monoclinic phase fraction. (b) Calculated monoclinic phase fraction and corresponding values of remanent polarization P_r as a function of film thickness. [4].

2.5 Negative Capacitance

It is important to know how regular capacitance functions so that one may understand the term and meaning of negative capacitance. This section will therefore be divided into two parts where the first one will cover regular capacitance and the second one will describe negative ones.

2.5.1 Regular Capacitance

When one speaks of capacitance it is referred to how much electric charge that can be stored in a component for a given change in voltage. Capacitance is a factor of geometry and can be both sought after or unwanted depending on the application. The simplest way of realizing capacitance is through a parallel plate capacitor, in which there are two conductive layers separated by an insulating dielectric layer.

Regarding planar MOSFET structures they can be regarded to have the parallel plate capacitor structure where the gate contact and electron channel are the upper and lower conductive layers respectively. In between these there is an insulating layer made out of high-k dielectric e.g HfO_2 which blocks Direct Current

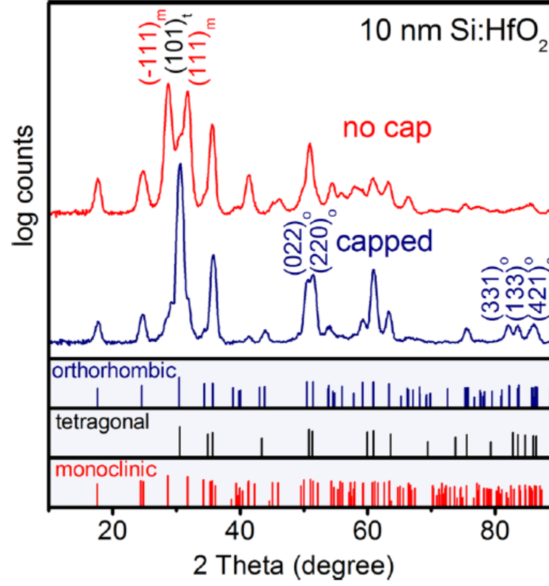

Figure 2.10: Grazing incidence x-ray diffraction measurements of two Si:HfO2 samples of the same composition where crystallization was induced with and without capping. [5].

(DC) current from passing through. The capacitance of a parallel plate capacitor is calculated from equation 2.4 where ϵ_r is the relative permittivity, ϵ_0 is the vacuum permittivity, A and d are the area of the plates and the distance between them. For the MOSFET this will correspond to the thickness of the gate oxide and the area of the channel and gate.

$$C = \frac{\epsilon_r \epsilon_0 A}{d} \tag{2.4}$$

From 2.4 it is understood that a dielectric with a high ϵ_r enables a thicker layer while still maintaining the same capacitance. This thereby reduces the risk of leakage and breakdown.

When the MOSFET operates there is a voltage difference between the gate and the substrate in the on-state of an nFET. The gate is more positive than the substrate which causes an electric field. This accumulates positive charges on the gate electrode whereas negative charges are accumulated below the dielectric in the channel to compensate the positive gate charge. This is what creates the conductive channel between the source and drain and is absolutely crucial for operation. Due to this it is of highest importance that the dielectric does not break down and keeps its insulating property. Owing to the electric field over the dielectric it becomes polarized. This is schematically depicted in figure 2.11.

The ideal capacitor is a purely reactive device containing zero resistive effects, meaning there is no power dissipation. When doing a P-E measurement of an ideal capacitor a linear relationship (see figure 2.12) should occur between the applied

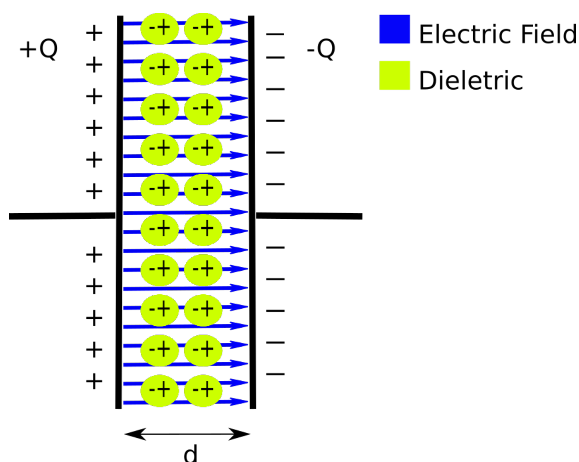

Figure 2.11: Schematic of a parallel plate capacitor with polarization of the dielectric, where Q denotes the charge and d the plate separation.

electric field and the polarization. This differs from a ferroelectric material which, as mentioned earlier, looks like in figure 2.13 where there is a hysteresis curve present.

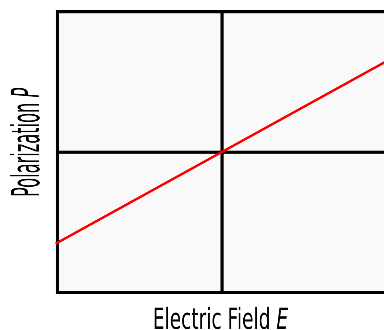

Figure 2.12: P-E curve of a ideal capacitor.

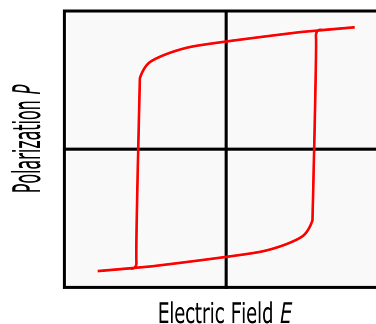

Figure 2.13: Hysteresis of a ferroelectric material.

The use of high-k dielectrics enables higher capacitance at the same thickness as regular dielectrics preventing current leakage while simultaneously improving oxide breakdown. This has enabled further down scaling of the MOSFET structure and in today's transistors high-k dielectrics play a crucial part of the performance.

2.5.2 Negative Capacitance

The attraction in implementing negative capacitance in transistors is to bypass the 60mV/decade *SS* restriction for MOSFETs in order to make them more efficient and reduce the operational voltage. In order to solve this the idea is to use

a ferroelectric material of the appropriate thickness to amplify the gate voltage via a step-up voltage transformer [14]. Thus the channel well "feel" a stronger gate voltage than is actually applied. This voltage transformer can be seen as the result of effective negative capacitance. The physics behind this can be understood by analyzing phase transitions in ferroelectric dielectrics. It is important to emphasize that there is no such thing as an absolute negative capacitance. Instead when one talks about negative capacitance it is referred to as "negative diffrential capacitance" where it is only negative in the transition region, see figure 2.14.

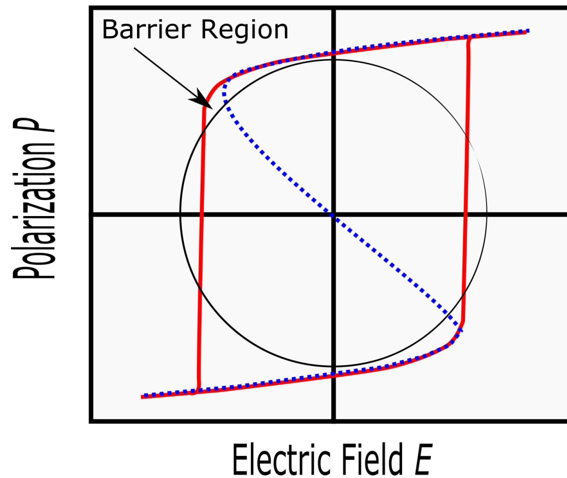

Figure 2.14: Schematic of Hysteresis curve for a ferroelectric material where the red curve denoted the measured, turquoise the accurate polarization where the negative differential capacitance is present in the barrier region.

The phenomena of negative capacitance stems from stored energy of phase transitions in a material [37] however the ability to measure and observe the phenomenon is limited. Due to the two degenerate states mentioned previously (see figure 2.4) for a ferroelectric material it is possible for the material while in non-equilibrium to show negative differential capacitance [14] [38].

The state where negative capacitance is achieved is a local maximum (barrier region) and is an unstable energy configuration for the system. However the state can be stabilized through a series dielectric capacitor [14]. This is the difficult part of integrating negative capacitance in transistors, since the state is unstable and has to be matched with the capacitance of the MOSFET. In particular since the MOSFET capacitance varies with bias it has proven difficult to achieve this matching.

2.6 MIM Cap Energy Band Theory & Leakage Mechanisms

In this section I will describe what happens in the oxide when an electric field is applied, using band theory. I will also mention the mechanisms giving rise to

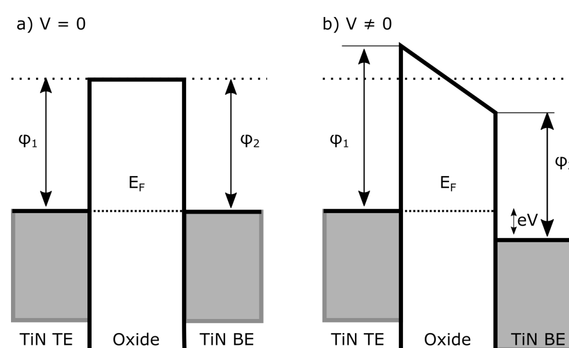

Figure 2.15: Schematic of energy band structure of MIM structure.

leakage in the oxide and how to analyze the data to determine if the mechanism is dominating.

2.6.1 Energy Band Theory of MIM Cap

When a bias is applied over the MIM capacitor structure a potential drop will arise across the oxide. Depending on the magnitude of this bias carriers in the TiN electrode will be attracted to the interface between the oxide and the metal. This potential shifts the energy bands close to the oxide. This increases the chance of electrons to tunnel through the potential barrier as well as enabling electrically active traps in the oxide to tunnel in and out of it. The effect is schematically shown in figure 2.15 where ϕ_1 and ϕ_2 are the work function of the metals and E_F the fermi level.

2.6.2 Tunneling & Leakage Mechanisms

The purpose of the oxide is as mentioned earlier to insulate and inhibit electrons from travelling from the channel to the gate electrode or vice verse. However there will always be some electrons passing through the oxide layer and this is what gives rise to leakage current. The leakage current is ideally due to direct tunneling which is a quantum mechanical effect in which electrons can penetrate through an energy barrier with a certain probability. In this section I will briefly cover the types of tunneling mechanism which are known to give rise to leakage currents through the dielectric oxide. When and why they occur will be discussed.

Direct Tunneling

Direct tunneling is a mechanism only present for very thin oxides. It arises from penetration of charge carriers directly through the oxide. For electrons there are two possible mechanisms. Tunneling from the valence band (VB) and tunneling from the conduction band (CB). For holes there is tunneling from the VB only.

Due to the difficulty of the direct tunneling mechanism several assumptions are required in order to quantify the contribution to the leakage current. Equation

2.5 displays a simplified model where the finite availability of charge carriers for tunneling has been neglected. From *Ranuarez* et al this model is adequate for oxides thicker than 2nm [39] .

$$J_{DT} = CE_{ox}^2 exp\left\{-\frac{4}{3}\frac{\sqrt{2m_{ox}^*}\phi_b^{3/2})}{\hbar q}\frac{1}{E_{ox}}\left[1-(1-\frac{qV_{ox}}{\phi_B})^{3/2}\right]\right\} \quad (2.5)$$

In 2.5 V_{ox} is the voltage applied across the oxide, E_{ox} is the electric field across the oxide, m_{ox}^* is the effective mass of electrons in the oxide ($= 0.5m_0$ [40]), ϕ_B is the effective barrier height (barrier height between the conduction bands at the interface of the SC-oxide), $\hbar$ is the reduced Planck constant, q is the electron charge and C is a constant.

Trap Assisted Tunneling

During an ideal deposition of the high-k dielectric there will be no defects in the oxide, unfortunately this is never the case. At some sites in the oxide layer there will be impurities, faulty bonds, an excess or deficit of oxygen atoms giving rise to defects. These defects create available states in the forbidden band gap of the oxide, states which often are electrically active. Defects with states that are electrically active have the ability to trap electrons or holes from the semiconductor deteriorates the performance of the oxide.

Trap assisted tunneling (TAT) arises from these active defects in the oxide layer. With increasing electric field and temperature the probability of holes or electrons tunneling to traps increases. When this happens the electron or hole then has a much greater probability of further tunneling to the gate metal since the energy required is reduced substantially.

The trap assisted tunneling mechanism can occur in two ways, either by single trap (STAT) or multi trap (MTAT). The only difference is if the charge carriers passes through one or several traps to permeate the dielectric [41]. It should be noted that MTAT only occurs for very poor oxides which are highly degraded.

TAT is a mechanism which contributes to leakage currents through the oxide at relatively low electric field but is also increasing with temperature due to a raise in thermal energy [42].

Fowler-Nordheim Tunneling

Fowler-Nordheim (FN) tunneling stems from the theory that electrons placed in a strong electric field can tunnel through a barrier in the direction of the applied field if the barrier is thin enough for the given electric field strength. Applying a strong electric field will shift the potential barrier of the metal downwards, this alters the potential barrier into a triangular shaped one which is thinner hence increasing the probability of electrons tunneling through it [43]. This will be the dominating tunneling effect for high electric fields.

Through some simplifications and assumptions it is possible to quantify the addition to the tunneling current caused by the FN effect. The contribution from FN is displyed in 2.6.

$$J_{FN} = CE_{ox}^2 exp\left[-\frac{4}{3}\frac{\sqrt{2m_{ox}^*}\phi_B^{3/2})}{\hbar q}\frac{1}{E_{ox}}\right] \quad (2.6)$$

This equation is applicable as long as the following assumptions are considered: the shape of the potential barrier is triangular and the electrons that have a possibility of tunneling can be described as a Fermi gas which are temperature independent. Plotting the logarithm of J_{FN}/E_{ox}^2 versus $1/E_{ox}$ will produce a straight line should the FN tunneling effect be the predominant leaking mechanism [39]. From the slope of the plot it is possible to derive the potential barrier height ϕ_B.

Poole-Frenkel Emission

While FN tunneling can be a dominating mechanism it implies that the carriers are free to move through the insulator. However this is not always true. For some oxides such as thermally grown SiO_2 the FN model is highly accurate but for oxides with a high density of defects such as silicon nitride the modeling using FN becomes inaccurate. This is due to the traps close to the band edge which provides the oxide with additional energy states. Since the traps captures and emits electrons the current flow becomes restricted. If the trap density is large enough this emission will become the dominating current mechanism through the oxide.

The model commonly used for PF emission is displayed in 2.7 where C is a constant proportional to the density of bulk oxide traps, q the elemental charge, k_B the Boltzmann constant, T the temperature, J_{PF} is current density attributed to PF emission, ϕ_t the trap energy level in the oxide and the other parameters are similar to those in 2.6.

$$J_{PF} = CE_{ox} exp\left[\frac{-q(\phi_t - \sqrt{qE_{ox}/\pi\epsilon_0\epsilon_r})}{k_B T}\right] \quad (2.7)$$

With the use of 2.7 and plotting $ln(J_{PF}/E_{ox})$ vs $E_{ox}^{1/2}$ the value of ϵ_r and ϕ_t can be extracted from the slope and interception with the y-axis of the plot respectively [44].

Schottky Emission

Schottky emission (SE) is the emission of an electron over a surface barrier and is considered a field-assisted thermionic emission. Meaning it is temperature and field dependent. The SE competes with the FN in the absence of a bulk limitation [43]. The expression for SE is displayed in 2.9

$$J_{SE} = A^* T^2 exp\left[\frac{-q(\phi_B - \sqrt{qE_{ox}/4\pi\epsilon_0\epsilon_r})}{k_B T}\right] \quad (2.8)$$

where

$$A^* = \left(\frac{4\pi q m^* k_B^2}{h^3} \right) \tag{2.9}$$

Which is the effective Richardson constant. m^* the effective electron mass in the oxide ($0.5m_0$ for HfO_2 [40]), ϕ_B is the Schottky barrier height and h is Planck's constant. For current passing through an oxide with the SE mechanism plotting $ln(J_{SE}/T^2)$ vs $E^{1/2}$ will be a straight line. From this ϕ_B and ϵ_r can be extracted via the intercept of the y-axis and the slope of the line [44].

The different types of current leakage mechanisms are graphically visualized in figure 2.16.

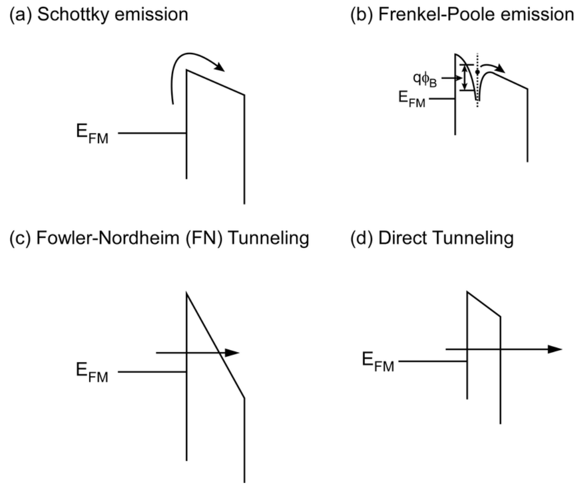

Figure 2.16: Tunneling mechanisms of insulators schematically displayed. Image taken from [6].

2.6.3 Dielectric Breakdown

When the oxide is put under high electrical stress the number of filled traps increases as well as additional conductive states can be generated. This only happens at sufficiently high biases and is often reversible. This increase in current during stress is known as stress induced leakage current (SILC) but is not a hard-breakdown. A model for this phenomena is proposed by Bersuker *et al* that suggests that the grain boundaries (GB) present conductive paths through the oxide. These paths arises from migration of doubly positively charged oxygen vacancies and their eventual segregation at the GBs. This is explained to form an extra sub-band within the dielectric energy gap [45]. These vacancies can then trap injected electrons and support TAT current. However when the voltage is removed the vacancies are reversed into doubly charged once again.

Pirrotti *et al* demonstrated that grains and GB heavily impact the oxides electron transport for poly-crystalline HfO_2. They showed with the use of conductive atomic force microscopy (CAFM) that the leakage current through a thin dielectric

film preferentially flows via the GBs [46]. It was also estimated that the density of defects are larger at the GB as compared with the grains which goes hand in hand with their CAFM measurements.

In order to decrease the SILC different approaches have been presented. Tackhwi *et al* presented a Dy-doped HfO_2 with a higher barrier height than pure HfO_2. The increased barrier height inhibits a further increase in the electron tunneling and trapped holes lessen the hole-tunneling currents heavily decreasing the SILC [47].

When the conduction path (believed to occur along GB) is created this is referred to as a dielectric breakdown. When breakdown occurs the leakage current increases severely and abruptly. However there are two types of breakdowns, soft and hard. The difference being the magnitude of the increased. It is believed that when a soft breakdown occurs a single conduction path is formed which yields a substantial increase in leakage current. When hard breakdown occurs the even further increased current is believed to come from the widening of the conductive path [48]. When breakdown occurs this permanently damages the oxide making it conductive instead of insulating.

2.7 Processing & Characterization Methods

In this chapter I will briefly cover the most important processing and characterization techniques used during the thesis. For information or interest in other methods used during this work please refer to Semiconductor Devices: Physics and Technology by Sze, S.M. and Lee, M.K. [49].

2.7.1 Atomic Layer Deposition

Atomic Layer Deposition (ALD) is a high accuracy thin film deposition technique and can be classified as a Chemical Vapor Deposition (CVD) process. ALD uses the gas phase of molecules to grow materials in a layer by layer fashion. It is a widely used technique in the semiconductor industry for depositing gate oxides due to its high accuracy. It provides excellent conformallity and uniformity along with rather simple and accurate control over film thickness [50]. The ability to deposit thin films over an entire wafer at once together with good reproducibility makes the ALD a great processing tool for industrial use.

The process uses precursors which sequentially react with the surface of the substrate to deposit the thin film. The process is schematically shown for growth of Aluminim Oxide (Al_2O_3) in figure 2.17 below. Initially trimethylaluminim (TMA) is added to the reaction chamber to react with the hydroxylated layer on the substrate. The TMA reacts with the surface releasing Methyl (CH_3) as the aluminum binds to the Oxygen (O). Using a carrier gas the excess TMA and methane is removed from the chamber. Then a short pulse of oxygen plasma is used where oxygen radicals reacts with methyl groups on the surface, binding to the alumina which generates Carbon monoxide (CO), Carbon dioxide (CO_2) and water molecules that are later removed using a carrier gas. Through these steps one atomic layer has been deposited. This process is repeated until desired thickness is acquired. However it should be noted that the exact substrate surface

outcome after plasma pulse is not as obvious as after regular thermal ALD and could deviate depending on the circumstances.

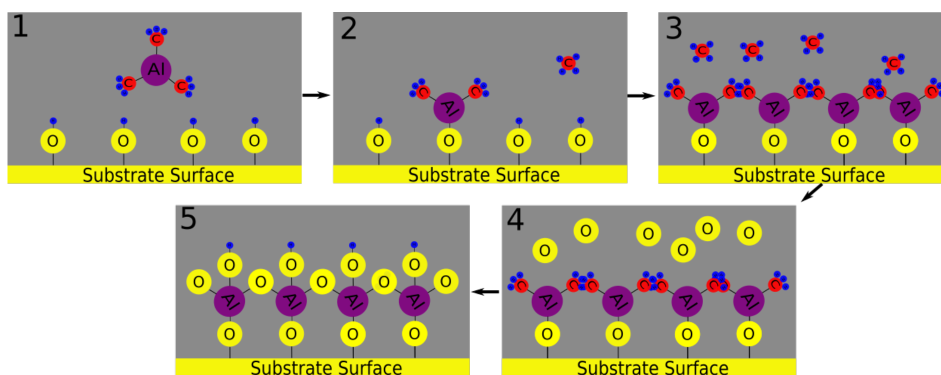

Figure 2.17: A schematic view of the ALD process for depositing Al_2O_3. (1) initiation of process, adding first precursor (TMA). (2) one TMA reacting with the surface oxide releasing CH3. (3) The excess TMA and methane are removed using a carrier gas or protrusion step. (4) A oxygen plasma pulse reacts with the surface. (5) One atomic layer Al_2O_3 deposited. Image modified from [7].

In this thesis I will use the Fiji F200 ALD system located in Lund Nano Lab (LNL) to grow HfO_2 films. A plasma enhanced ALD process will be used utilizing the precursor Tetrakis(ethylmethylamido)hafnium(IV) (TEMAHf). However all the surface reactions taking place during the plasma ALD process of HfO_2 with this precursor are not completely known. For the interested reader theories of the surface reactions during ALD of HfO_2 using TEMAHf is explained in [51] [52].

The benefit and purpose of using the plasma enhanced ALD instead of the thermal process is because it will enable lower processing temperature, give rise to a more uniform film due to the plasma's higher reactive properties and reduce purge and nucleation times [53].

2.7.2 Thermal Evaporation

Thermal evaporation is a very simple physical vapour deposition (PVD) process which most often utilizes a resistive heat source to evaporate metals in a vacuum environment. The heating along with the vacuum environment creates a high enough vapour pressure for the metal which makes it evaporate. This coats the substrate and produces thin metal films. Figure 2.18 shows a schematic of the evaporation chamber.

With the use of a shadow mask a selective areas of the sample can be coated making it a great technique for metal contacting. The shadow mask placement in the chamber can be seen in figure 2.18 as well.

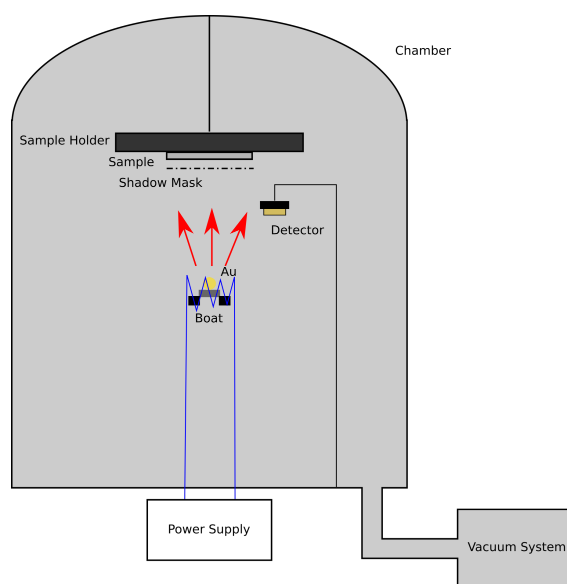

Figure 2.18: A schematic view of the evaporation chamber utilizing a shadow mask.

2.7.3 Ellipsometry

Ellipsometry is an optical technique to determine the thickness and refractive index of thin films. It measures the change in polarization of light in order to determine these properties. Ellipsometry is a very established characterization technique and has been used for several decades. There are articles from early 1960 describing the function of the ellipsometer and its benefits [54]. What makes ellipsometry the preferred technique for thin film measurements can be attributed to several factors. Firstly it can measure film thicknesses down to the subnanometer scale, it inflicts zero damage on the sample, has high accuracy and can be conducted at various environments [55]. Even more impressing is that it is an applicable technique for almost all types of materials. Semiconductors, metals, organics, superconductors, dielectrics, composites and biological coatings can be characterized with ellipsometry.

Ellipsometry is as mentioned based on optical polarization and the change of it. The polarization can be described as the light waves electrical field $\vec{E}$. The reason why polarization is important is due to the preferential directions of action for electric charges in a material when it is exposed to a light wave [56]. There are basically three types of polarization regarding light waves., linear, circular and elliptical. Where the most common polarization is elliptic polarization and this is where the name ellipsometry comes from. Elliptic polarization means that the x and y polarization components are of different amplitude and phase. Hence looking at the wave from a plane perpendicular to the propagation direction one will see an elliptical trajectory. Linear polarization is when two orthogonal waves are in phase whereas circular polarization occurs when the two waves are out of phase

with 90°but have the same amplitude. The polarization of light is summarized in figure 2.19.

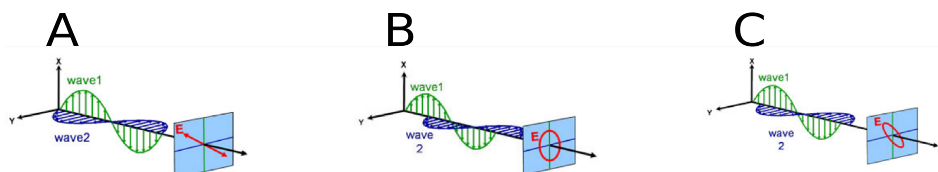

Figure 2.19: Different polarizations of light. ***A*** Linear, ***B*** Circular and ***C*** Elliptical. Image taken from https://www.jawoollam.com.

The following paragraphs will briefly explain the ellipsometry measurement procedure. In figure 2.20 a schematic of an experimental setup is displayed for clarification.

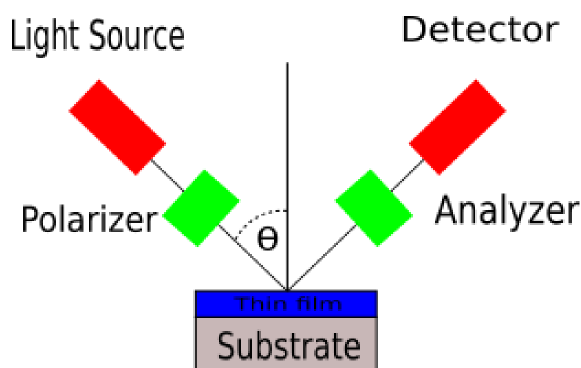

Figure 2.20: Schematic of experimental setup for ellipsometry measurements.

As the light leaves the light source it passes through a polarizer which linearly polarizes the emitted light. It then reaches the sample where it is reflected. Ellipsometry is a specular optical technique and thus the reflection angle is the same as the incidence angle. After reflection it hits a second polarizer shown in figure 2.20 as "analyzer" and lastly it reaches the detector.

The measured signal is denoted the complex reflectance ratio ρ which is parameterized by the amplitude ratio ψ and the phase difference Δ. The light wave that hits the sample can be divided into two components, parallel and perpendicular to the plane of incidence. These are known as p- and s-polarizations [56]. After reflection and normalization the amplitudes of the p- and s-polarization are denoted r_P and r_S and named complex reflectivities. Ellipsometry measures the ratio between r_P and r_S which is denoted the complex reflectance ratio . This is often expressed using ψ and Δ as seen in equation 2.10. Where $tan(\Psi)$ is the amplitude ratio upon reflection, Δ is the phase shift. Additionally ellipsometry

measures the ratio and hence the difference of r_P and r_S rather than the absolute value, which yields very high accuracy of the technique.

$$\rho = r_P/r_S = tan(\Psi)e^{i\Delta} \tag{2.10}$$

A very important step for ellipsometry is the data analysis where the measured diffraction is put in to an analysis model. In order to quantify the values of Ψ and Δ the Jones and Mueller matrix methods are the most common ones used. How these work will not be covered in this work, for further interest please see [55]. Since ellipsometry is an indirect method a regression type analysis is required since an exact equation cannot be expressed. After measuring a model is generated which describes the present sample. With the use of this model the Fresnel's equation response is calculated which describes the reflection and refraction of light at planar interfaces. The experimental data is compared to the calculated theoretical data from the model. By changing unknown material properties to improve the match between theoretical and experimental values the best match is achieved. With the use of regression the Mean Square Error (MSE) minimum is found [57]. From this procedure properties of the material can be determined.

2.7.4 Atomic Force Microscopy

Atomic Force Microscopy (AFM) is a commonly used characterization method to determine and image the roughness of surfaces and layers, with resolution down to single atoms. The technique was proposed already in 1986 by Binnig et al [58]. The AFM technique has become popular due to the wide range of materials able to use it. Since it is applicable to conductive and insulating surfaces it has attracted chemists, biologists, physicians, physicicsts, mechanical engineers and many more [59]. Providing detailed information about height distributions and surface roughness it has become the go-to technique for characterizing morphology.

The following paragraph will briefly describe the principles behind the AFM, what it measures and how this information is interpreted. For a more thorough explanation please refer to *Meyer* in [59] or *Binnig* et al in [58].

The atomic force microscope setup contains a probe tip, cantilever spring, an xyz-directional moving stage, sample holder, deflection sensor and sometimes a feedback loop [59]. In figure 2.21 a schematic AFM setup is shown.

Measurements begin with placing the sample in the holder and scanning over the sample surface in the x and y directions by moving the stage. While scanning the sample the deflection between the tip and the sample in the z-direction is measured by the deflection sensor. Due to small spring constants down to 0.001N/m and the ability to register tiny motions down to 0.1Å by the deflection sensor at small forces (10^{-11}N) non destructive imaging is possible. The AFM can operate in two modes - contact and non-contact mode. The difference being the distance between the sample and the probe tip. The non-contact mode enables measuring forces such as magnetic, capillary, electrostatic and van der Waals. This grants information regarding charge distribution, magnetic domain wall structures, topography and liquid film distribution [59]. Switching to contact mode where the tip touches the sample as it is swept over the surface this allows for the ionic

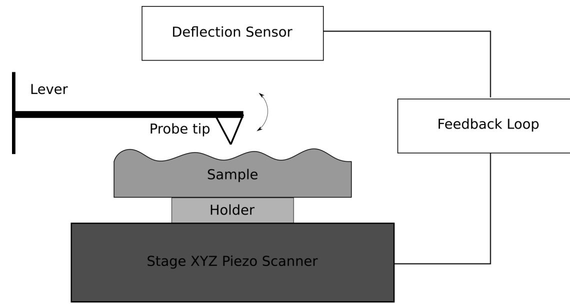

Figure 2.21: Schematic of experimental setup for an atomic force microscope.

repulsion forces to be determined. This mode gives rise to even higher resolution and in the best case scenario permits single atomic resolution.

Analysis of the AFM images grants information of the surface roughness. The most commonly used metric when analyzing the surface is the arithmetical mean deviation of the assessed profile Ra defined as

$$Ra = \frac{1}{n}\sum_{i=1}^{n}|y_i| \tag{2.11}$$

Another frequently used metric is the Root mean square value (RMS or Rq) defined as

$$Rq = \sqrt{\frac{1}{n}\sum_{i=1}^{n}y_i^2} \tag{2.12}$$

for more on this topic please refer to [60].

Chapter 3

Fabrication & Calibration

This chapter will cover the steps done to fabricate the Metal-Insulator-Metal (MIM) devices that were characterized in this thesis. This includes various techniques such as wet etching, sputtering, evaporation, rapid thermal annealing and atomic layer deposition. All sample processing and development was conducted in the Lund Nano Lab, LNL, at Lund Univesity.

3.1 Sample Fabrication Process

3.1.1 Cleaning of Wafer

The initial substrate used in this thesis is a heavily p-doped (boron) silicon 4 inch wafer with a thick oxide layer of SiO_2. Due to the layer of SiO_2 on the wafer a wet etch was required before any film deposition was possible. The wafer was etched in Buffered Oxide Etch (BOE) for five minutes in order to remove the oxide. The duration was determined by the surface becoming hydrophobic. The wafer was then put in deionized water for two minutes and afterwards it was dried using a nitrogen gun. This process is displayed schematically in figure 3.1.

Figure 3.1: Schematic of the sample after etching of SiO_2.

3.1.2 Deposition of Bottom Electrode

After cleaning the wafer the bottom electrode was deposited. TiN was sputtered onto the substrate using the AJA Orion 5 tool in LNL. The silicon wafer was mounted onto the sample holder and put into a ventilated load lock, after which the load lock is sealed and pumped down to a pressure of $< 10^{-6}$bar. After transferring the wafer into the deposition chamber RF sputtering was carried out with a power of 150W. A pre-cleaning procedure of the target for 5 minutes was used before opening of the magnetron shutter. Sputtering for 600 seconds with a deposition rate of 0.16nm/s yielded a layer of $\sim$10nm titanium nitride as bottom electrode. Figure 3.2 presents a schematic view of the sample at this stage.

Figure 3.2: Schematic of the sample after TiN BE sputtering.

After sputtering of the TiN bottom electrode the wafer was divided into smaller samples and put in storage boxes specific to their corresponding sample series. For every sample series there will be one parameter changing in the growth process of the hafnia film while the other paramaters remain constant.

3.1.3 Hafnia Deposition

With the TiN bottom electrode in place the deposition of the high-k dielectric took place. This was done with the Fiji F200 ALD system. Several samples series were grown and the following paramaters were altered

- Plasma Duration
- Plasma Power
- Deposition Temperature
- Oxygen Flow
- Plasma Purge time

Finally a sample was grown where the optimized parameters of previous growths were applied. The complete deposition conditions for all samples are summarized in chapter 5.

Figure 3.3 displays a schematic of the sample after this step of the process.

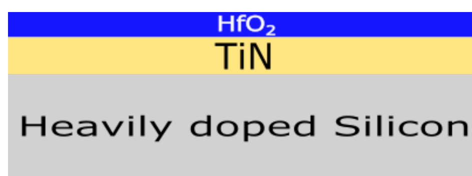

Figure 3.3: Schematic of the sample after HfO_2 deposition.

After this point the samples were split in two. If the electric characterization of the first piece turned out well (good electrical characteristics) the second piece could be annealed and its ferroelectric behaviour evaluated.

3.1.4 Top Electrode Deposition

Next step involves deposition of the TiN top electrode. This took place in the same manner as for the bottom electrode. Using the AJA Orion 5 sputter to deposit

a 10nm thin top electrode of titanium nitride. The same process conditions was used as for the bottom electrode where a 5 minute pre-clean of the target was applied and the samples were exposed to sputtering for 600 seconds.

Figure 3.4 displays a schematic of the sample as far, having deposited the bot and top electrode of TiN as well as the high-k HfO_2 dielectric of the MIM structure.

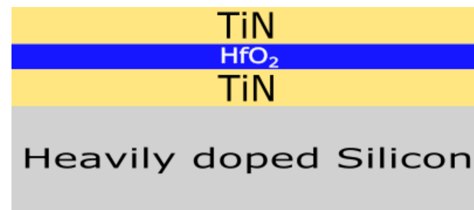

Figure 3.4: Schematic of the sample after top layer capping with TiN.

3.1.5 Annealing Process

In order to crystallize the amorphous HfO_2 film a rapid thermal annealing step was implemented where the samples were spike annealed to a temperature of 650°C for 30 seconds. The fastest heating rate possible (estimated to 100-150°C/s) by the RTP-1200-100 system from UniTemp GmbH was used along with the quickest cooling rate, with the purpose of minimizing the thermal budget of the samples. The HfO_2 films are expected to go from amorphous to polycrystalline after the RTP process.

3.1.6 Metal Contacting

In order to conduct measurements on the samples a thicker 200nm highly conducting top metal out of Gold (Au) was deposited using a thermal evaporation technique. However due to poor adhesion after annealing a 5nm layer of titanium was evaporated underneath. The thickness of deposited gold is crucial for the sample since it will protect the underlying structure (the dielectric) during electrical measurements and counteract the probes from penetrating the dielectric film. The evaporation was done in the AVAC system in LNL utilizing a shadow mask with circular patterns with diamaters ranging from 50-200 μm. The pattern from the shadow mask is displayed in figure 3.6. The dimensions and notation of the circles are marked in the image as well. A deposition rate of 1nm/s and a pressure of $1.6 \cdot 10^{-6}$ was used. A schematic view of the sample after the evaporation process is shown in figure 3.5.

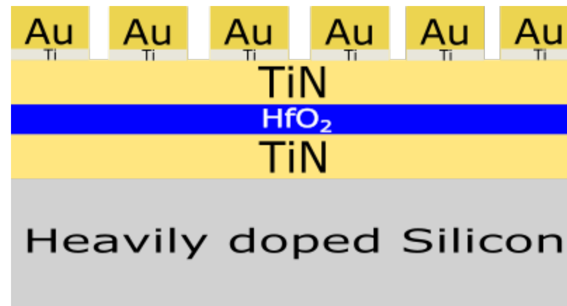

Figure 3.5: Schematic of the sample after evaporation.

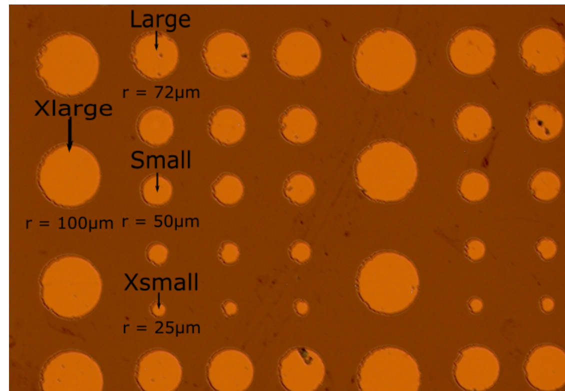

Figure 3.6: Optical spectroscopy image of fabricated sample after metal deposition.

3.1.7 Etching the Top Contact

As one can see from figure 3.5 the bottom electrode of titanium nitride is short circuiting the capacitors and therefore needs to be partially removed. With the use of a wet-etchant it is possible to selectively etch away the TiN not covered by the top TiN/Au spots. The samples were therefore wet etched in a solution of ammonium hydroxide (NH_4-OH), hydrogen peroxide (H_2O_2) and deionized water (H_2O) with the ratio 1:2:5 (APM). The solution was prepared as follows. 25ml deionized and purified water was added to a beaker along with 5ml of ammonium hydroxide solution. The solution was then heated to a temperature of 60°C using a hotplate. At the time of reaching 60°C 10ml hydrogen peroxide was added to the solution. The addition of hydrogen peroxide somewhat decreased the temperature of the solution. The solution was once again heated to 60°C and kept at this temperature for the etching. At this temperature the solution has a known vertical and side etching rate of 1.07nm/s and 0.45nm/s respectively [61].

The samples were etched in the APM solution at 60°C for a duration of 30 seconds and then put in a beaker with deionized water. Since the structures are very big (radius of 25-100 μm) compared to the thickness of TiN the undercut

from lateral etching is negligible. It was therefore preferred to "overetch" in order to make sure that there was no residual TiN on the surface short circuiting the capacitors. In figure 3.7 a schematic view of the sample is displayed after the etching step. This was the final step in processing of the capacitor structures and measurements could now be conducted.

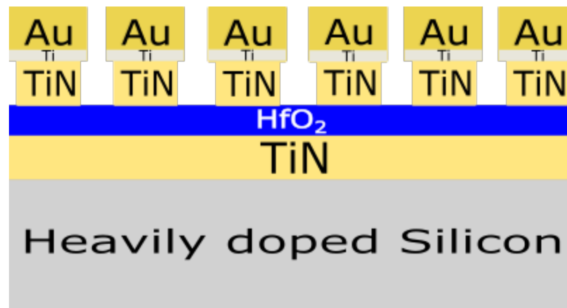

Figure 3.7: Schematic of the sample after TiN etching.

To summarize this chapter a step by step schematic of the process is shown in figure 3.8.

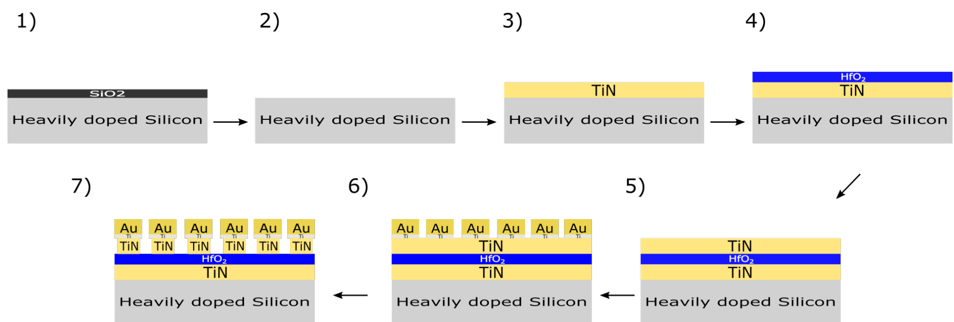

Figure 3.8: Schematic of the entire sample process step by step.

3.2 TEMAHf Calibration

Due to a new source for deposition of hafnia in the Fiji F200 ALD system, calibration of the ALD process was required. The new TEMAHf requires different growth conditions compared to the previously used TDMAHf source due to their different chemical properties. In order to find adequate growth conditions for the new source several paramaters were varied and the impact of these were analyzed.

Since the TEMAHf source has a low vapour pressure, heating of the precursor jacket is required. In order to achieve the same vapour pressure as with the old TDMAHf source (operating at a temperature of 75°C) a temperature of roughly 110-115 °C is needed [61] [62]. With this in mind the temperature of the source was set to 113°C.

A first test run was conducted in order to see whether the set temperature was enough to achieve adequate vapour pressure to deposit a uniform film - which it was. The next parameter to alter was the precursor pulse time, this to make sure that a fully saturating dose was pulsed into the chamber every cycle. In order to measure this samples were placed as displayed in figure 3.9 covering the entire deposition surface. This was done for every run as the pulse length was varied between 0.05s and 0.9s.

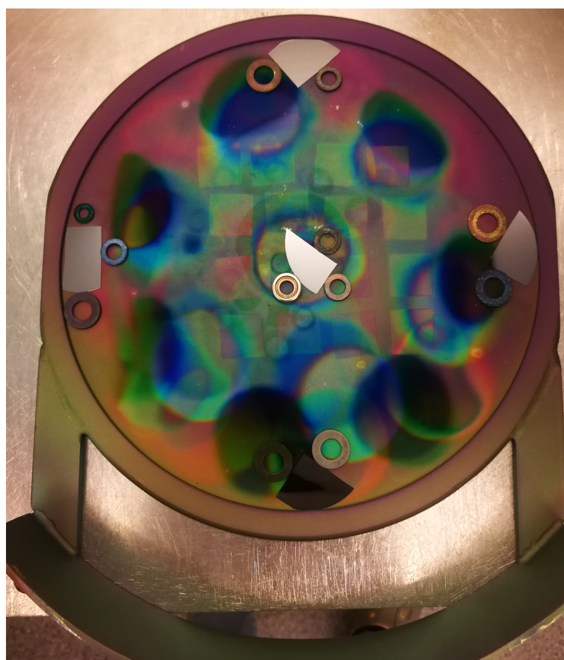

Figure 3.9: Sample placing on the chuck of the ALD.

After finding a suitable value for the pulse length the impact of the purge time after precursor pulsing was investigated. According to *Haussmann* et al [62] when the purge time is less than sufficient the Growth per Cycle (GPC) increases. When the purge time is to short there will be residues left in the chamber between pulses. Residues which can react with the pulsed precursor during gas phase and cause contamination to the sample. Therefore runs where made where one sample was placed in the middle of the chamber and the purge time was varied between 0.1s up to 7s.

When the deposition temperature becomes to high decomposition of the precursor will occur. In order to avoid this the thermal stability was evaluated. *Haussmann* et al [62] found that at temperatures of 400°C or more the TEMAHf experiences thermal decomposition [62]. Since the process for depositing hafnia in this thesis will be based on temperatures below 300°C this will not cause any issues.

Every sample was characterized using ellipsometry to determine the thin film thickness and the refractive index of the films. Since the films grown are very thin

(below 100nm), and the models for the ellipsometer is based on bulk hafnia, a thicker 200nm reference sample was grown at first. From this sample a new model was generated using a Cauchy optical model in order to fit the measured data. All samples were then measured using this generated Cauchy model.

Chapter 4

Electrical Characterization Method

In order to evaluate the device performance and confirm certain properties characterization is necessary. This is done by evaluating leakage currents using ordinary I-V curves and P-E measurements. To be able to draw conclusions from these measurements knowledge of the sample structure and composition is critical thus AFM, optical spectroscopy and Ellipsometry measurements is performed as well. This chapter introduces the different benchmarking metrics and how they are obtained.

4.1 Leakage Current

The evaluation of leakage current for the MIM structures was done by applying a voltage over the capacitor and measuring the current through it. This provides information regarding the leakage current, the breakdown voltage and breakdown field. This was done using the 11000B Cascade probe station with a Keithley 4200A parameter analyzer. One probe and a coaxial cable was used. The probe was connected to the top metal of the MIM structure whereas the coaxial cable was connected to the chuck of the probe station. The voltage was then swept in different ranges depending on the thickness of the sample.

4.2 Polarization-Electric field Measurement

By doing a polarization measurement one will get information regarding the domains in the film, since these can shrink, grow and switch due to the external electric field applied. The measurement is conducted by measuring the relative polarization while sweeping the applied electric field over the capacitor. From these results it is possible to determine whether the HfO_2 is ferroelectric, anti-ferroelectric or simply dielectric.

The measurement was done using a setup as displayed in figure 4.1 where a periodic voltage signal is applied across the capacitor and the current through the capacitor is measured and converted to a voltage using a Stanford Low noise current preamplifier model SR570. The measured signal is compared to the reference signal from the function generator and through some data analysis in MATLAB the P-E curves can be achieved. This method is known as the "Virtual Ground"

method and is commonly used for ferroelectric samples. The theory behind this method is described below.

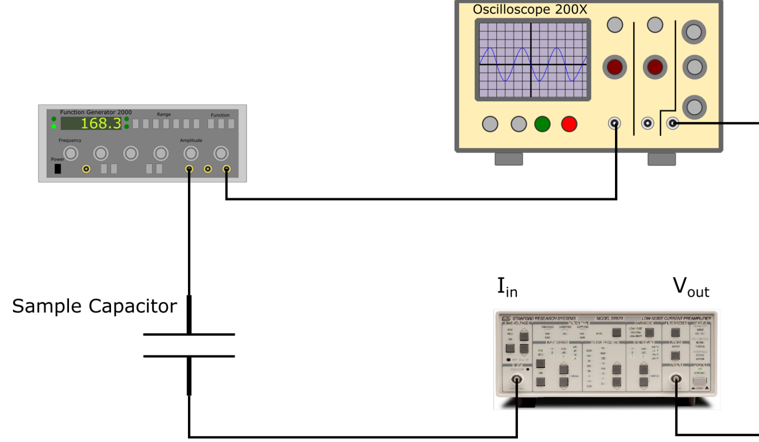

Figure 4.1: Measurement setup for P-E.

With the use of a triangular voltage signal a variation in the current through the capacitor is achieved. By measuring this current through the device it is possible to calculate the stored charge of the sample at a given time t. This is done with the numerical integration of the current *I=I(t)*.

$$Q(t) = \int_{t_1}^{t_2} I dt \tag{4.1}$$

The dielectric displacement D is calculated as the surface charge density [63].

$$D(t) = \frac{Q(t)}{A} \tag{4.2}$$

For high permittivity ferroelectrics the polarization P at a given time is almost equal to the dielectric displacement D. This yields

$$P(t) = \frac{Q(t)}{A} \tag{4.3}$$

where A = area of sample (in our case a circle where A = πr^2). Hence by measuring the current through the capacitor and evaluation of the numerical integral in 4.1 the polarization P can be calculated as a function of the applied field E_{ox} [63].

From the "Virtual ground" measurement setup the dielectric constant ϵ_r can be derived as follows. With the current measured and the derivative of the input signal determined the capacitance can be calculated through

$$I = C\frac{\partial V}{\partial t} \tag{4.4}$$

Since our device is a parallel plate capacitor the capacitance is

$$C = \frac{\epsilon_0 \epsilon_r A}{d} \Rightarrow \epsilon_r = \frac{Cd}{\epsilon_0 A} \tag{4.5}$$

where A is the area of the device, d is the thickness of the dielectric and ϵ_0 is the vacuum permittivity.

Chapter 5

Results & Analysis

5.1 TEMAHf Calibration in Fiji F200

From calibration of the new source the impact on GPC was evaluated for several paramaters. In figure 5.1 the GPC and refractive index is shown for hafnia growth where the oxygen flow was turned on and off for every deposition cycle in the ALD process. The GPC dependence for varying pulse times (figure 5.1a) and purge times (figure 5.1c) are presented. With the use of a Woollam M2000VI ellipsometer the thickness of the films and refractive index was determined. For the measurements a Cauchy model was implemented and the films were scanned using wavelengths of 400-900nm with the incidence angles of 70, 75 and 80 degrees to fit the data. and fitting a Cauchy model for ALD grown HfO_2.

There is only a negligible difference in GPC depending on the sample placement in the deposition chamber and is observed exclusively for low pulse lengths. From this data it is evident that the entire chamber is being saturated for the pulse times used. However for maximum repeatability samples should be placed at the same spot in the chamber for every deposition.

From figure 5.1a it can be seen that the GPC has saturated at a pulse length of roughly 0.65 second and this value was therefore used in all the following depositions. In figure 5.1c the GPC is seen to rapidly increase at purge times below 1 second. This can be explained by by-product remains not being fully purged out of the chamber which leads to reactions in vapour phase. This leads to the thin film loosing its uniformity which is what is seen for purge times below 1s at the given temperature of 200°C.

According to the literature values of the refractive index at $\lambda \approx 600nm$, are between 1.95-2 [52, 64], which corresponds quite well with the measured values in this thesis ($n \approx 2.1$) where negligible variation is found depending on pulse times.

Due to the low reactivity and vapour pressure of the TEMAHf precursor it was decided to investigate whether the precursor would react with the oxygen gas or not. This was done with the goal of removing stabilization times of the oxygen flow each cycle and thus shortening the overall deposition time. A deposition on a test sample (a 2" silicon wafer) was carried out where O_2 gas was supplied during the entire ALD process, including the precursor dose. The plasma was not ignited for the the deposition. From this test it was verified that no growth took place on the test sample and therefore it was concluded that the precursor TEMAHf

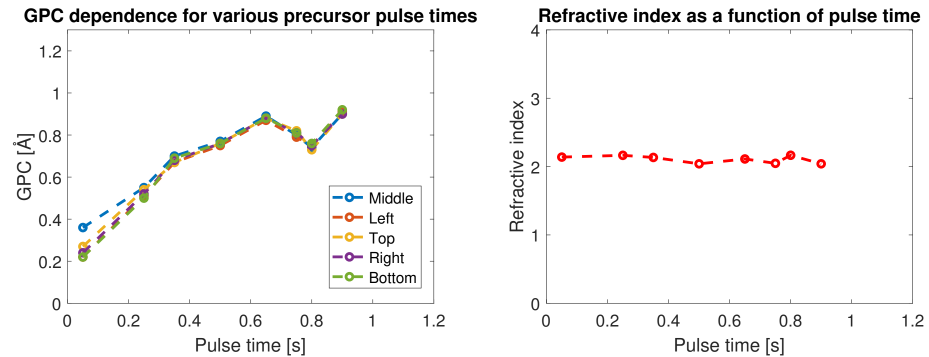

(a) GPC dependence on pulse time for different placements in the deposition chamber.

(b) Refractive index dependence on pulse time for $\lambda = 600nm$.

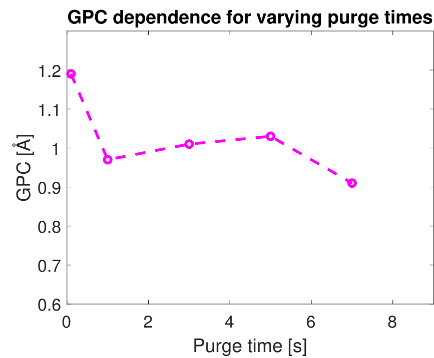

(c) GPC dependence on purge times.

Figure 5.1: Calibration of GPC for TEMAHf source in Fiji F200 ALD.

does not react with the molecular oxygen gas at the given conditions. From these results the presence of parasitic CVD components can be excluded [65]. This had a huge impact on the recipe run time where the duration of the growth cycle could be decreased from approximately 36 to 26 seconds yielding an almost 30% faster cycle time. However new GPC measurements were needed in order to verify the GPC and refractive index.

In figure 5.2 the GPC and refractive index is displayed for hafnia growth where a constant oxygen flow was applied through the entire ALD process. The GPC dependence for varying pulse and plasma duration are shown in figure 5.2a and figure 5.2c respectively.

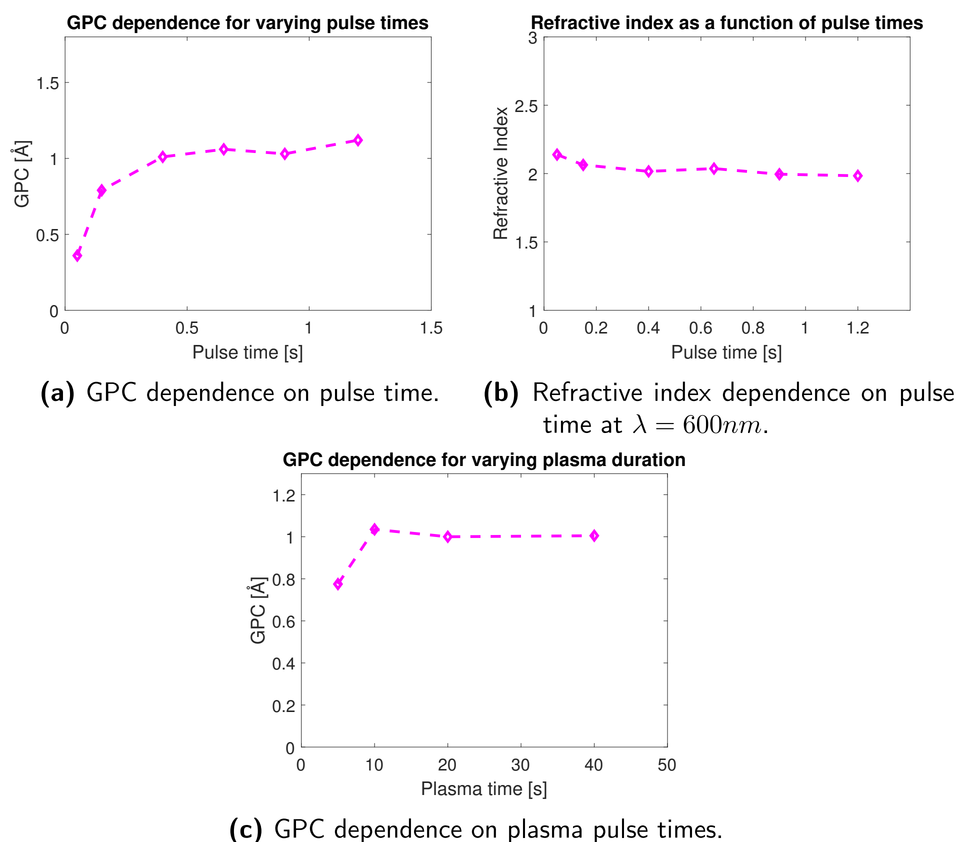

(a) GPC dependence on pulse time.

(b) Refractive index dependence on pulse time at $\lambda = 600nm$.

(c) GPC dependence on plasma pulse times.

Figure 5.2: Calibration of GPC for TEMAHf source in Fiji F200 ALD.

From this data one can see that saturation in GPC is reached for pulse lengths above ~ 0.4s which gives a GPC of around 1.05Å. By supplying oxygen flow during the entire recipe saturation of GPC is achieved for shorter pulse length and the saturation in GPC is more pronounced. The GPC is slightly higher as well for corresponding pulse lengths. It is also clear that a plasma time of at least 10 seconds is required in order to reach a saturated GPC. As before the refractive index is as to be expected, ~ 2 and very tiny variations are observed.

5.2 Sample Series Specifications & Electrical Characterization

In this section I will describe the different HfO_2 samples series that were grown. The complete process conditions, what paramaters were altered and why is presented. Following the growth conditions is the data measured from the electrical characterization of the samples.

The general recipe structure from previous recipes for HfO_2 in the Fiji F200 ALD system in LNL was applied at first, see appendix B. For the first sample

series, denoted 1, the duration of the active plasma was varied. Samples of 20nm were grown where the plasma duration ranged from 5s to 80s. The deposition conditions for these samples are summarized in 5.1.

Table 5.1: Deposition conditions of sample series 1.

Process Conditions					
Sample	**1**	**2**	**3**	**4**	**5**
Plasma Duration [s]	**5**	**10**	**20**	**40**	**80**
Pulse time [s]	0.65	0.65	0.65	0.65	0.65
Purge time 1 [s]	5	5	5	5	5
Purge time 2 [s]	0	0	0	0	0
Oxygen Flow [sccm]	20	20	20	20	20
Temperature [°C]	200	200	200	200	200
Plasma Power [W]	300	300	300	300	300
Cycles	40	40	40	40	40

where "purge time 1" is the purge time after precursor delivery and "purge time 2" is the purge time after turning off the plasma. Results from the electrical characterization of these samples are presented below.

Figure 5.3 displays I-V characteristics for capacitors of different sizes and varied plasma duration. From this data it was clear that the smallest size capacitor possessed the most favourable characteristics, having the lowest leakage currents. This observation was in line with the expectations since these devices have the smallest area prone to defects. It was therefore decided that all following measurements were going to be conducted on capacitors of the smallest size ($\sim 25\mu m$ radius).

Examining figure 5.3d a general trend presented itself where longer plasma duration resulted in lower leakage currents independent of the capacitor size.

From figure 5.4 the normalized leakage current at 1V, J_{1V}, is shown. Unfortunately sample 1 of this series grown with 5s plasma duration only had too leaky devices and was thus removed. The data shows a very clear trend of decreasing leakage current with increasing plasma duration. Figure 5.4a shows the breakdown voltage V_{bd} where a vast increase is noted for longer plasma times. It is reasonable to expect that the oxygen content of the HfO_2 increases with increasing plasma duration and since some vacancies are desired for ferroelectricity a plasma duration of 20s was selected for further samples.

The use of W as a top contact was attempted with the hopes of being able to sputter the entire structure in a single step, thus eliminating the TiN etching step in the process. For two samples W was sputtered as a top contact instead of gold.

One can very clearly see that for the exact same sample there is a big difference between using W or Au as a top contact. Higher J_{1V} values, lower V_{bd} values and a larger spread in the data was observed for the W top contact. The reason for this is at the moment unclear and it was not further investigated in this work. Finally it must be noted that even though the leakage current decreased and the

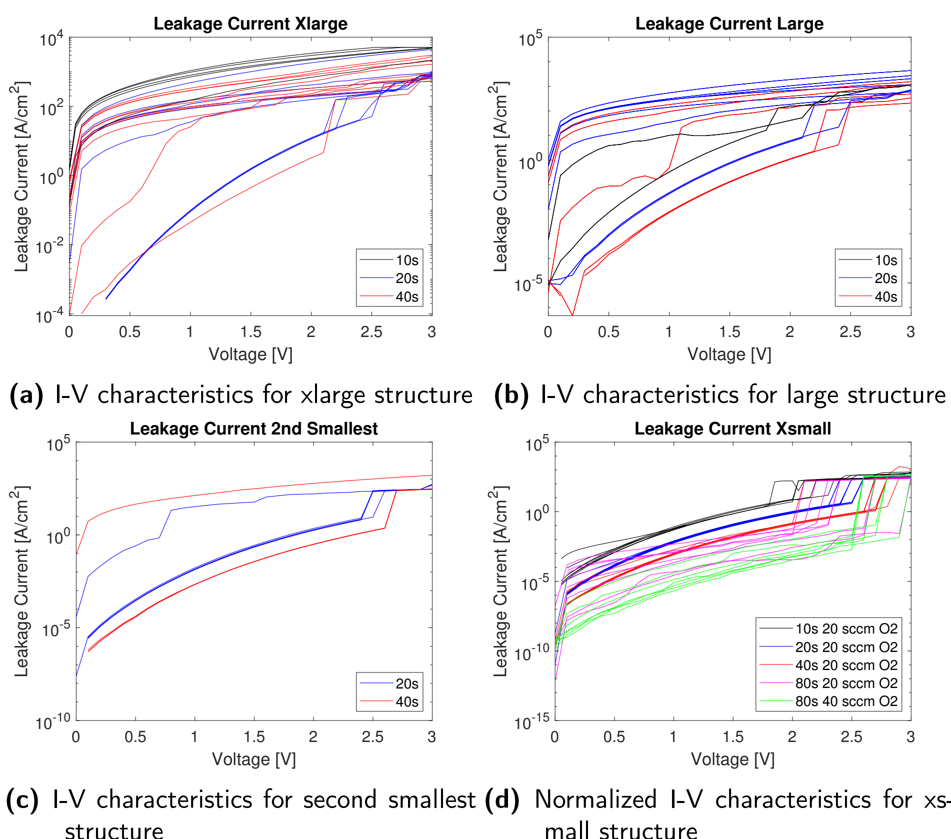

(a) I-V characteristics for xlarge structure

(b) I-V characteristics for large structure

(c) I-V characteristics for second smallest structure

(d) Normalized I-V characteristics for xsmall structure

Figure 5.3: I-V characteristics for sample series 3 of different device area. 4nm HfO_2 deposited with varying plasma pulse duration.

breakdown voltage increased with increasing plasma duration so did the spread in the data.

It was believed that in the same way as altering the plasma duration to change the oxygen concentration in the film it would also be possible to do this by adjusting the plasma power. The plasma power was altered in series 2 between 50 and 300W. 5.2 summarizes the ALD process conditions for the second sample series.

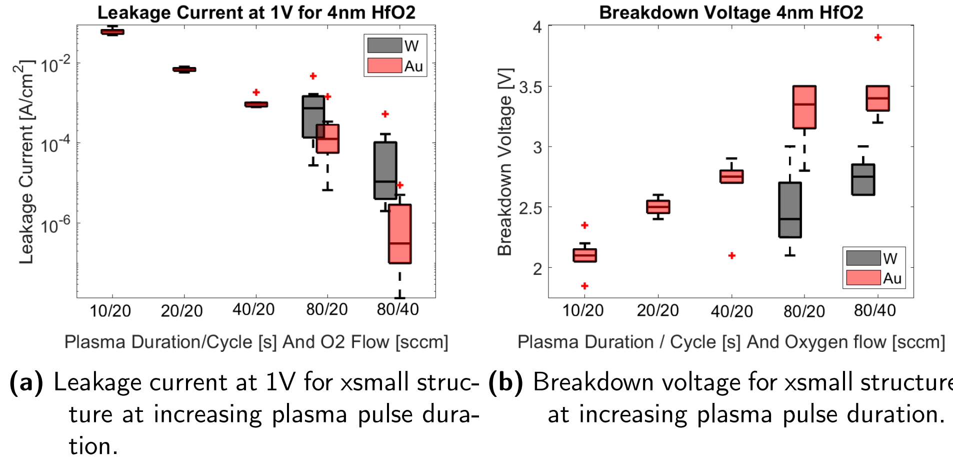

(a) Leakage current at 1V for xsmall structure at increasing plasma pulse duration.

(b) Breakdown voltage for xsmall structure at increasing plasma pulse duration.

Figure 5.4: Leakage current at 1V and breakdown voltage for xsmall structure of 4nm thin HfO_2 with increasing plasma duration.

Table 5.2: Deposition conditions of sample series 2.

Process Conditions				
Sample	**1**	**2**	**3**	**4**
Plasma Duration [s]	20	20	20	20
Pulse time [s]	0.65	0.65	0.65	0.65
Purge time 1 [s]	5	5	5	5
Purge time 2 [s]	0	0	0	0
Oxygen Flow [sccm]	20	20	20	20
Temperature [°C]	200	200	200	200
Plasma Power [W]	**50**	**100**	**200**	**300**
Cycles	40	40	40	40

The data from electrical characterization measurements is presented in figure 5.5. Where figure 5.5a shows the I-V characteristics, figure 5.5b the J_{1V} and figure 5.5c the V_{bd}.

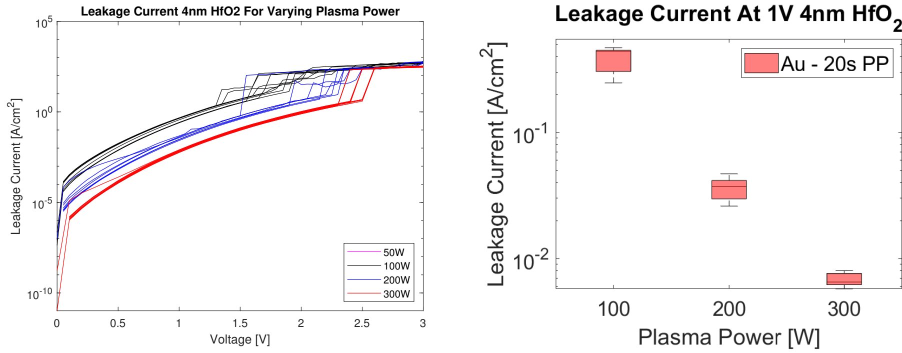

(a) J-V characteristics for xsmall structure at increasing plasma power.

(b) Leakage current at 1V for xsmall structure at increasing plasma power.

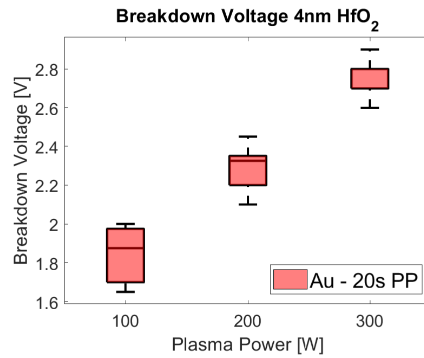

(c) Breakdown voltage for xsmall structure at increasing plasma power.

Figure 5.5: Impact on I-V characteristics, leakage current at 1V and breakdown voltage for xsmall structure of 4nm thin HfO_2 due to increasing plasma power.

The sample with 50W plasma power did only bear devices with too high leakage currents and thus did not provide any useful data. It is reasonable to expect that the film quality of this sample was too poor. The data in figure 5.5 is a clear indication that higher plasma power was beneficial. This yielded both lower leakage currents as well as higher breakdown voltage for the thin films. This can be explained through increasing oxygen concentration and thus decreasing the oxygen vacancies in the film which correlates with the previous results regarding plasma duration. Reducing the plasma power requires longer plasma duration in order to maintain the same oxygen concentration and since the plasma duration was fixed at 20s the samples with decreased plasma power (100W and 200W) has more vacancies and thus more defects which impacts the film in a negative manner.

As a third sample series the deposition temperature was varied since *Kim et al* showed in 2016 that it plays a fundamental role for the FE properties of undoped hafnia [66]. Films with a suitable thickness for ferroelectric hafnia of ∼8nm (80 cycles) thickness were grown with deposition temperatures ranging from 200 to 280°C. The processing conditions for sample series 3 are summarized in Table 5.3.

Table 5.3: Deposition conditions of sample series 4.

Process Conditions				
Sample	**1**	**2**	**3**	**4**
Plasma Duration [s]	20	20	20	20
Pulse time [s]	0.65	0.65	0.65	0.65
Purge time 1 [s]	5	5	5	5
Purge time 2 [s]	0	0	0	0
Oxygen Flow [sccm]	20	20	20	20
Temperature [°C]	**200**	**220**	**240**	**280**
Plasma Power [W]	300	300	300	300
Cycles	80	80	80	80

The electrical measurement data from these samples are shown in figure 5.6. The impact of the deposition temperature on I-V characteristics, J_{1V} and V_{bd} is presented in figure 5.6a, figure 5.6b and figure 5.6c respectively.

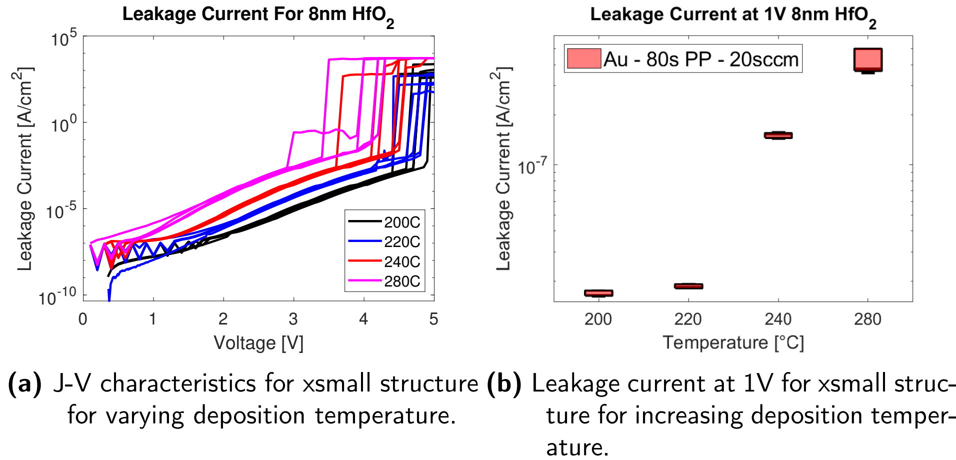

(a) J-V characteristics for xsmall structure for varying deposition temperature.

(b) Leakage current at 1V for xsmall structure for increasing deposition temperature.

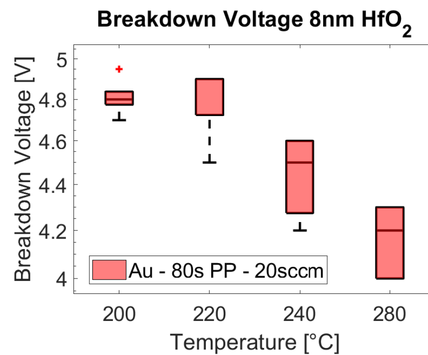

(c) Breakdown voltage for xsmall structure for increasing deposition temperature.

Figure 5.6: Impact on J-V characteristics, leakage current at 1V and breakdown voltage for xsmall structure of 8nm thin HfO_2 with respect to varying deposition temperatures.

Contrary to what *Kim* et al who observed reduced leakage for high deposition temperature we observe leakage current increase drastically for T $>$ 220°C. At T $>$ 220°C the V_{bd} degardes as well. One reason for this might be that the purge and pulse lengths have been optimized for 200°C and at temperatures above this the purge time is too long which leads to precursors breaking their bond to the substrate. Another less likely reason could be that decomposition of the precursor occurs which *Kim* et al found at 280°C and above for the TEMAHf precursor. However there seems to be several findings on this and according to *Hausmann* et al decomposition of TEMAHf does not occur until a temperature of 400°C [62]. From the clear trend shown in the data a temperature of 200°C was determined to be the most optimal.

Table 5.4: Deposition conditions of sample series 4.

Process Conditions				
Sample	**1**	**2**	**3**	**4**
Plasma Duration [s]	20	20	20	20
Pulse time [s]	0.65	0.65	0.65	0.65
Purge time 1 [s]	5	5	5	5
Purge time 2 [s]	0	0	0	0
Oxygen Flow [sccm]	**20**	**40**	**100**	**200**
Temperature [°C]	200	200	200	200
Plasma Power [W]	300	300	300	300
Cycles	40	40	40	40

The ferroelectric properties in undoped hafnia is believed to come from oxygen vacancies in the oxide [67]. It was therefore of interest to vary the oxygen flow during deposition in order to determine its impact on the film quality. Hence in series 4 the oxygen flow was altered between 20-200sccm during deposition. The deposition conditions for sample series 4 are presented in Table 5.4.

Figure 5.7 displays the data acquired from the electrical characterization measurements conducted on these samples. Where figure 5.7b shows the J_{1V} and figure 5.7c the V_{bd}.

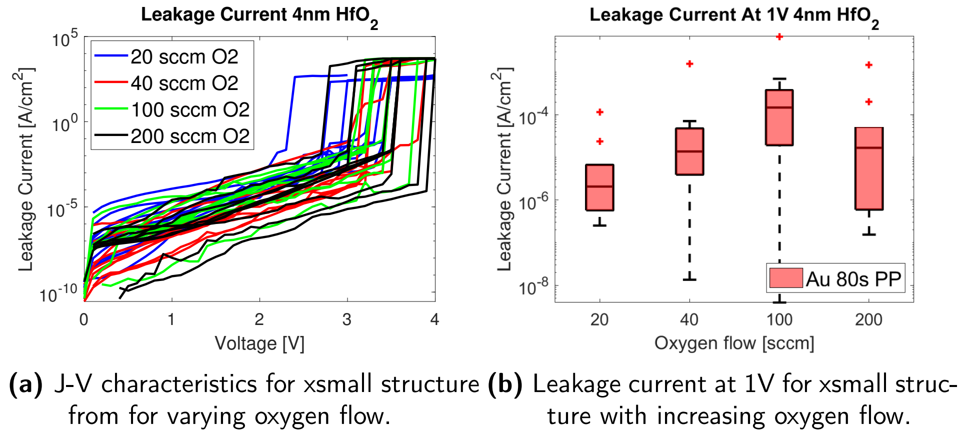

(a) J-V characteristics for xsmall structure from for varying oxygen flow.

(b) Leakage current at 1V for xsmall structure with increasing oxygen flow.

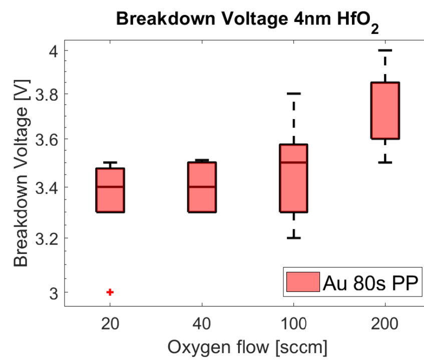

(c) Breakdown voltage for xsmall structure at increasing oxygen flow.

Figure 5.7: Impact on J-V characteristics, leakage current at 1V and breakdown voltage for xsmall structure of 4nm thin HfO_2 with respect to varying oxygen flow.

From this data it is very difficult to draw any conclusions about the impact on leakage currents. It can be seen that for oxygen flows above 20 sccm the spread of the data in both J_{1V} and V_{bd} seems to increase. Yet it does seems like the highest oxygen flow of 200 sccm gives rise to higher V_{bd}. However this comes with an increase in the spread of the data as well. A similar observation was made for increased plasma power and plasma duration as well.

Finally as the last parameter to tweak the purge time after the plasma step was evaluated (purge time 2). The purge time was varied from 0-5s for the samples. Complete deposition conditions for this series are shown in Table 5.5.

Table 5.5: Deposition conditions of sample series 5.

Process Conditions			
Sample	**1**	**2**	**3**
Plasma Duration [s]	20	20	20
Pulse time [s]	0.65	0.65	0.65
Purge time 1 [s]	5	5	5
Purge time 2 [s]	**0**	**2**	**5**
Oxygen Flow [sccm]	20	20	20
Temperature [°C]	200	200	200
Plasma Power [W]	300	300	300
Cycles	40	40	40

In figure 5.8 the data for the J-V characteristics, J_{1V} and V_{bd} is presented.

From the data in figure 5.8b it is visible that a purge time of 0 seconds clearly degrades the performance of the film and leakage current increases. This is believed to arise from vapor phase reactions of unreacted precursor and by-products. Utilizing a 2 second purge time after the plasma appears to be the best choice for minimizing the J_{1V}. Regarding the V_{bd} little to no difference is found for 0 and 2 seconds however a 5 second purge increases the V_{bd}. Nonetheless the spread vastly increased for this sample making the data quite indecisive.

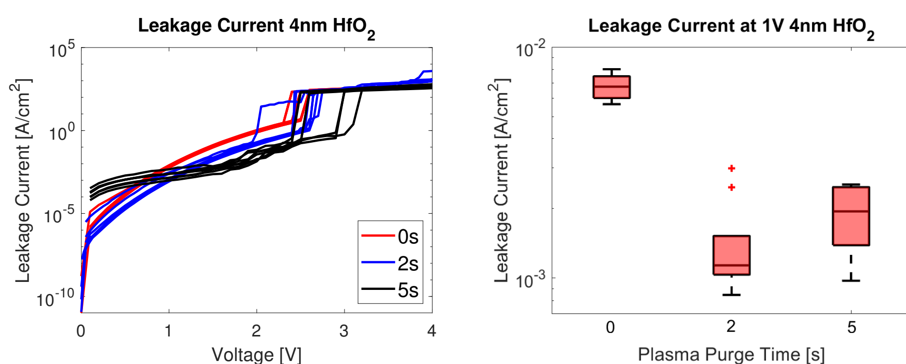

(a) J-V characteristics for xsmall structure for varying plasma purge duration.

(b) Leakage current at 1V for xsmall structure for increasing plasma purge duration.

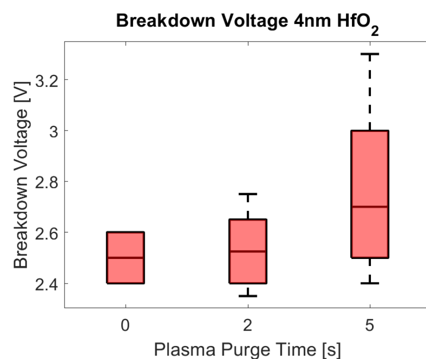

(c) Breakdown voltage for xsmall structure for increasing plasma purge duration.

Figure 5.8: Impact on J-V characteristics, leakage current at 1V and breakdown voltage for xsmall structure of 4nm thin HfO_2 with respect to varying plasma purge duration.

With the calibration of the ALD process window finished, a sample with the optimized parameters were grown. It was originally supposed to be a series of varying thickness but due to the TEMAHf precursor running empty only one sample could be fabricated. The fabrication parameters used for this sample are provided in Table 5.6.

Table 5.6: Deposition conditions of optimized sample ("series 6").

Process Conditions	
Sample	**OPT1**
Plasma Duration [s]	80
Pulse time [s]	0.65
Purge time 1 [s]	5
Purge time 2 [s]	2
Oxygen Flow [sccm]	40
Temperature [°C]	200
Plasma Power [W]	300
Cycles	100

In figure 5.9 the data from the electrical characterization is presented. Figure 5.9a displays the J-V characteristics, figure 5.9b the normalized leakage current at 1V, J_{1V}, and figure 5.9c the V_{bd}.

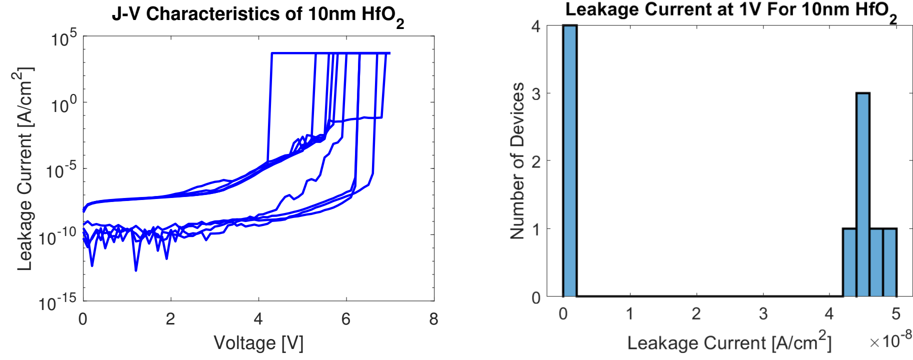

(a) I-V characteristics for xsmall structure for optimized sample.

(b) Leakage current at 1V for xsmall structure for optimized sample.

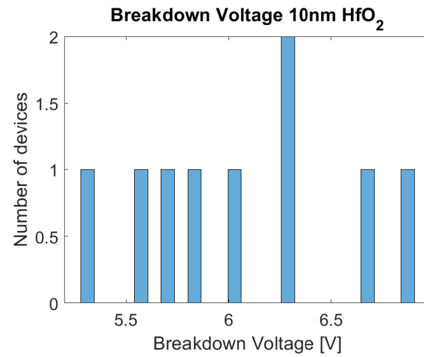

(c) Breakdown voltage for xsmall structure for optimized sample.

Figure 5.9: I-V characteristics, leakage current at 1V and breakdown voltage for xsmall structure of 10nm thin HfO_2 with optimized growth conditions.

The magnitude of leakage currents are in line or better with previous work done by Winqvist for the Savanna thermal ALD system in LNL [42]. From the J-V plot it seems that there are two groups of capacitor devices present with one group of devices exhibiting vastly lower leakage current by a factor of up to 100. One can also find that the breakdown field E_{bd} of this optimized sample is in the range of $\sim 5 - 7MV/cm$ which is substantially below the $\sim 9 - 11.3MV/cm$ shown for thermally grown HfO_2 in the Savannah ALD [42]. From previous results regarding plasma pulse, plasma power and oxygen flow it has been verified that the increase in oxygen concentration of the HfO_2 thin film boosts the V_{bd}. With this in mind it is believed that the oxygen concentration of the HfO_2 films grown in the Fiji F200 ALD is still less than the films grown in the Savannah ALD even at these "optimized" conditions. Despite lower V_{bd} for the films grown in the Fiji

F200 ALD the measured magnitude of $\sim 5 - 7$ MV/cm is considered enough for the application of the films as gate dielectric in transistors.

5.3 Effective Potential Barrier Height

5.3.1 Plasma Duration Series

In order to have valid P-E curves the leakage current values need to be low in comparison to the polarization current otherwise this will obscure the ferroelectric properties of the ferroelectric material. Due to the importance of low leakage currents it was considered valuable to analyze the J-V characteristics of the samples and determine the dominating leakage current mechanisms. Figure 5.10 displays different ways of analyzing the J-V characteristics according to the models mentioned in section 2.6.

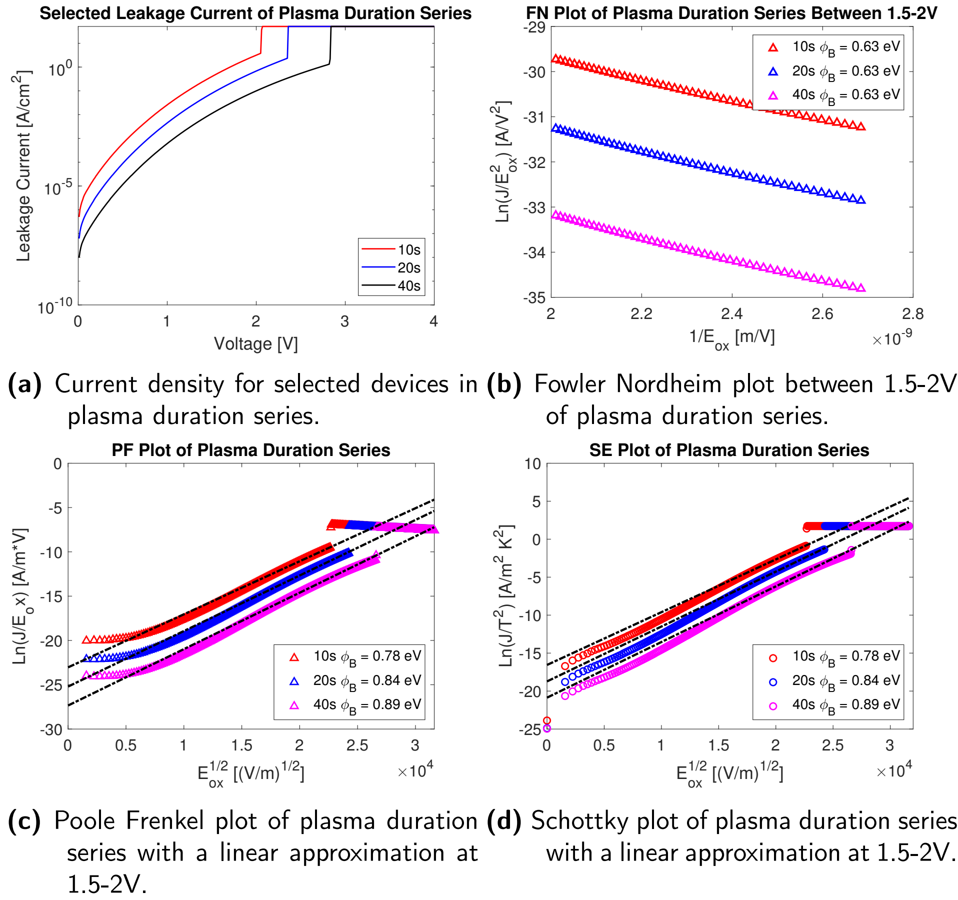

(a) Current density for selected devices in plasma duration series.

(b) Fowler Nordheim plot between 1.5-2V of plasma duration series.

(c) Poole Frenkel plot of plasma duration series with a linear approximation at 1.5-2V.

(d) Schottky plot of plasma duration series with a linear approximation at 1.5-2V.

Figure 5.10: (a) Current density, (b) FN, (c) PF and (d) Scottky plots of plasma duration series.

In figure 5.10a J-V characteristics of selected devices with three different plasma durations are presented. By utilizing the FN model and plotting J_{FN}/E_{ox}^2 versus $1/E_{ox}$ (figure 5.10b) for a bias between 1.5-2V it is noteworthy that the samples have the same slope and thus experience no change in barrier height ϕ_B.

With the use of equation 2.6 the potential barrier height ϕ_B is derived from the slope of the plot yielding $\phi_B = 0.63eV$. Since the carriers must tunnel through the insulator the criteria of $E_{ox}d \geq \phi_B$ has to be satisfied. A criteria which is fulfilled in this case.

In figure 5.10c the PF plot is shown where $ln(J_{PF}/E_{ox})$ has been plotted vs $E^{1/2}$. In the plot a linear approximation has been made in the bias range of 1.5-2V and with the use of equation 2.7, the slope and intersect of this line gives the dielectric constant ϵ_r and the trap energy level ϕ_t. From equation 2.7 and with the slope = 0.00064, ϵ_r is found to be ~ 24. For the calculations of ϕ_t a simplification has been made where C will be neglected (=1) since the density of states in the conduction band is unknown. This simplification is made possible since only the relative values between samples are of interest and not the absolute value. The intersects of the curves are found to be -23, -25 and -27 which corresponds to a trap energy level ϕ_t of 0.59eV, 0.65eV and 0.70eV.

The value of ϵ_r is according to literature in line with the expectations for HfO_2 [68] [8]. Regarding the trap energy level ϕ_t it appears that the increased leakage current for shorter plasma duration might stem from traps located at lower energy. This would also explain the very equal J-V characteristics in figure 5.10a.

Finally plotting $ln(J_{SE}/T^2)$ vs $E^{1/2}$ the SE plot is acquired, see figure 5.10d. A linear approximation has been made between 1.5V and 2V. It is clear in this representation as well that the different samples have very equal characteristics inheriting an equal slope of 0.00070. Furthermore, the intersects are derived to -17, -19 and -21 for red, blue and magenta respectively. Applying equation 2.9 the Schottky barrier height is calculated to 0.78eV, 0.84eV and 0.89eV as seen in the inset of figure 5.10d. The dielectric constant ϵ_r derived from the slope becomes $\epsilon_r = 4.4$. This value is very low for HfO_2 and based on this result the SE model is concluded to poorly represent the dominant leakage current mechanism.

Considering the data in figure 5.10 and the reasoning presented above the PF model seems to be the most appropriate model based on the extracted values for ϵ_r of ~ 24. It is therefore reasonable to expect that this is the dominating leakage mechanism in the oxide for these samples. The fact that we expect a high oxygen vacancy concentration in the films, further support the conclusion of PF being the main leakage mechanism.

5.3.2 Optimized Sample

In this section the same analysis as for the plasma duration series will be conducted. However in this case the optimized sample as-deposited will compared with the annealed sample of the same growth. Figure 5.11 presents the J-V characteristics (figure 5.11a), FN plot (figure 5.11b), PF plot (figure 5.11c) and the SE plot (figure 5.11d) for the samples.

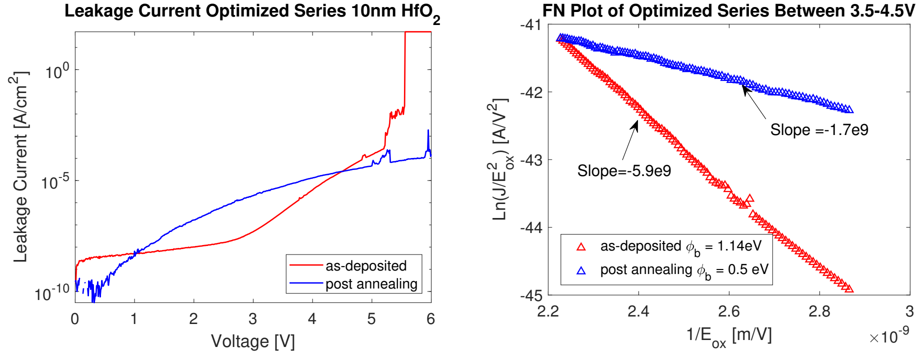

(a) Current density for optimized sample. **(b)** Fowler Nordheim plot of optimized sample.

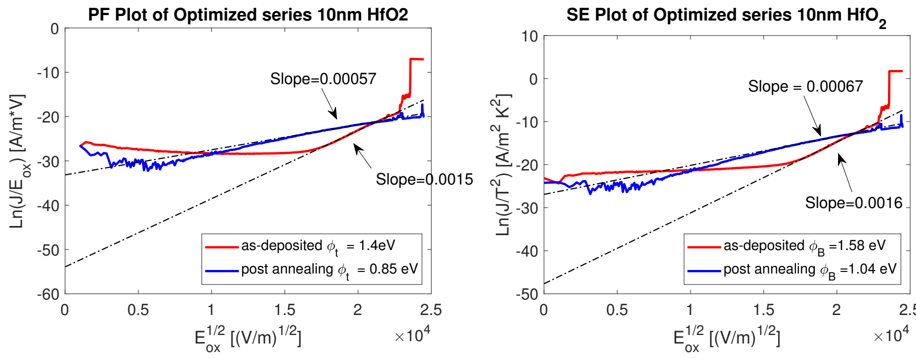

(c) Poole Frenkel plot of optimized sample. **(d)** Schottky plot of optimized sample.

Figure 5.11: (a) Current density, (b) FN, (c) PF and (d) Schottky plots of optimized sample as deposited and post annealing.

From figure 5.11a there is a clear difference in the J-V characteristics between the annealed and as-deposited sample. Indicating that there are different leakage mechanisms dominating for the two samples. The annealed sample has a very similar characteristic to the J-V curves from the plasma duration series samples with a rather quick and exponential increase in leakage current. Whereas the as-deposited sample responds as a ideal capacitor at lower bias keeping a rather constant leakage current until $\sim$ 2V. Above 2V the current increases exponentially until a soft breakdown occurs at $\sim$ 5V and a then a hard breakdown at approximately 5.5V. Corresponding to a breakdown field of $E_{bd} = 5.5MV/cm$.

By analyzing the FN plot in figure 5.11b and deriving the potential barrier height ϕ_b from the slope and using equation 2.6, one finds that ϕ_b for the as-deposited and annealed sample is 1.14eV and 0.5eV respectively. This corresponds well with the observation from the J-V plot where the annealed sample has a higher leakage current as a result of a lower potential barrier for the electrons to tunnel through. A potential reason for the lower barrier height is the increased diffusion across the TiN/HfO_2 junction after annealing, which is known to increase the trap density and lower the effective work-function [69].

Moving on to the PF model the PF plot is presented in figure 5.11c along with a linear approximation between 3.5-4.5V. The slope of the approximation is displayed in the figure as well. In the same way as for the FN plot except applying 2.7 instead, the trap energy level ϕ_t and the dielectric constant ϵ_r can be derived. For these calculations the same simplification has been made where C will be neglected (=1) since the density of states in the conduction band is unknown. Once again, this simplification is acceptable since only the relative values are of interest for the samples and not the absolute values.

From the slopes of 0.0015 and 0.00057 it is found that ϵ_r is $\sim$ 3.65 and $\sim$ 27 for the as-deposited and annealed sample respectively. From the intersect ϕ_t is calculated to 1.4eV for the as-deposited sample and 0.85eV for the annealed one. These finding are very interesting since this implies that for the as-deposited sample having a $\epsilon_r \sim 3.65$ the PF model is not very accurate. Thus this is likely not the dominating leakage mechanism for the sample. Yet for the annealed sample the PF model fits very well with an $\epsilon_r \sim 27$. Owing to the high ϵ_r this could indicate a successful suppression of the monoclinic phase ($\epsilon_r = 16$) in the oxide. Meaning a higher concentration of higher dielectric constant crystal phases of HfO_2 is present. Regarding the trap energy level ϕ_t no comparison between the samples can be made since the PF model does not fit the data for the as-deposited sample.

Finally, the SE plot by plotting $ln(J_{SE}/T^2)$ (T = 300K) vs $E^{1/2}$ is presented in figure 5.11d with a linear approximation at 3.5-4.5V (linear region). From this the Schottky barrier height ϕ_B and the dielectric constant ϵ_r can be derived from the intersect with the y-axis and the slope of the linear region. The slopes are calculated to 0.0016 and 0.00067 for the as deposited and annealed sample respectively. With the use of equation 2.9 ϵ_r becomes $\sim$ 0.84 for the as-deposited HfO_2 and $\sim$ 4.8 for the annealed one. The intersects with the y-axis are determined to -47 and -28. From these values and using 2.9 ϕ_B is derived. The Schottky barrier of the annealed sample is calculated to 1.04eV and the as-deposited sample $\phi_B = 1.58eV$.

Using the SE model grants very low values of the dielectric constant (0.84 and 4.8) which gives an indication that this probably is not the dominating leakage current mechanism.

The results derived using the different models are summarized in 5.7. With these results and the arguments presented above the PF model seems to be most accurate leakage mechanism for the annealed sample with a dielectric constant of 27. Whereas for the as-deposited sample the only model fitting the data somewhat accurately is the Fowler-Nordheim model. This would indicate a transition from a low defect film and FN tunneling to a more defect rich HfO_2 after annealing in which PF dominates.

Table 5.7: Summary of results from analysis of the J-V characteristics using FN, SE and PF models.

	FN		PF		SE	
	ϵ_r	ϕ_b [eV]	ϵ_r	ϕ_t [eV]	ϵ_r	ϕ_B [eV]
As-deposited	-	1.14	3.65	1.4	0.84	1.58
Post Annealing	-	0.5	27	0.85	4.9	1.04

5.4 Atomic Force Microscopy

Evaluation of sample topology and roughness was done using atomic force microscopy in order to determine the Rq (RMS) and Ra values of the deposited film. For further information on how this is done please read the theory section of AFM in section 2.7.

With the use of Bruker AFM Icon AFM images of the optimized sample was taken. In figure 5.12 2D and 3D AFM images are presented. Images were taken over a large area (figure 5.12b & figure 5.12d) of 3x1.5μm and a smaller area (figure 5.12a & figure 5.12c) of 500x250nm.

From the AFM images the surface topology is visualized. The biggest distance between a peak and valley is determined to $\sim$4nm which is quite high considering the total HfO_2 thickness of 10nm. The Ra value defined from equation 2.11 of the film was calculated to 0.487nm and the Rq value attained from equation 2.12 was 0.620nm. This yields an RMS of approximately 6.2%. This value is considered moderately high which would suggest a rough film. For dielectric films deposited using the ALD process during good conditions a RMS of $<$1% is generally achieved for smooth films [62]. However consideration must be taken to the underlying structure of the hafnia film. Below the film there is TiN deposited using sputtering, a process measured and evaluated by AFM to have a RMS value of 1.06nm. This indicates that the observed roughness comes from the sputtering process and that the ALD process of HfO_2 actually decreases the surface roughness. Due to this it is seems reasonable to believed that the roughness observed in the AFM images comes from a rough topology of the underlying structure and not the HfO_2 film itself.

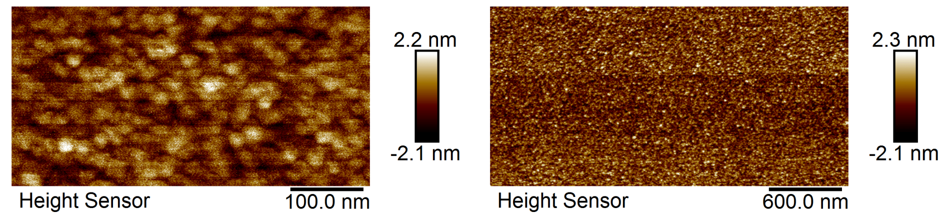

(a) AFM image of 500x250nm area.

(b) AFM image of 3x1.5μm area.

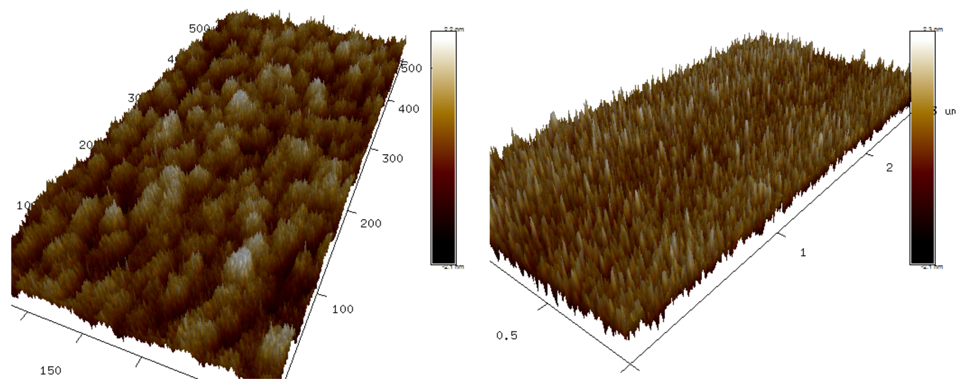

(c) 3D-AFM image of 500x250nm area.

(d) 3D-AFM image of 3x1.5μm area.

Figure 5.12: 2D and 3D AFM images of HfO_2 of the optimized sample for small and large areas.

5.5 P-E Measurements

The results from the P-E measurements done using the Virtual Ground method (see measurement section) is shown in figure 5.13 where the blue line is the triangular input signal and the orange one the measured voltage. This was done for three devices of the optimized sample annealed at 650°C. In the same figure the polarization vs electric field curves are also plotted. The polarization is derived from equation 4.3 described in section 4.2. Finally with the use of equations 4.4 and 4.5 the dielectric constant as a function of electric field is presented.

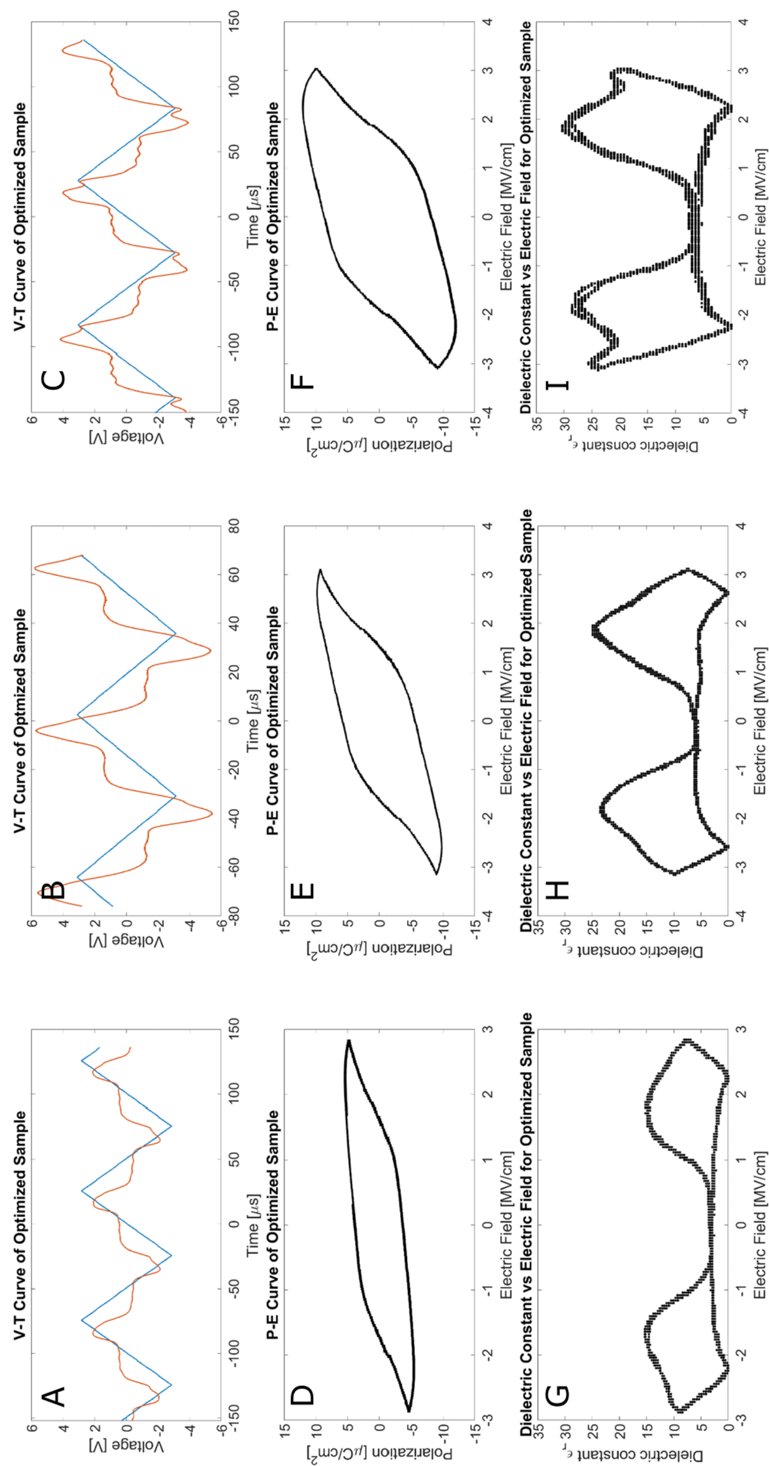

Figure 5.13: (A-C) V-T, (D-F) P-E and (G-I) ϵ_r-E curves of three different devices from the optimized sample with an area of ~1.4e-5 cm^2

The samples OPT1:A,B,C are measured at a frequency of 10, 15 and 18 kHz respectively. Values of the remanent polarization P_r, coercive field E_c and ϵ_{max} are summarized in table 5.8.

Table 5.8: Summary of metrics derived from P-E measurements.

P-E Measurement Results			
Sample	**OPT1:A**	**OPT1:B**	**OPT1:C**
P_r [$\mu C/cm^2$]	4.0	5.9	8.75
E_c [MV/cm]	1.65	1.53	1.8
ϵ_{max}	15.4	25	30

From this data it is evident that the hafnia films are ferroelectric, with clear hysteresis loops and varying dielectric constant. The values obtained for P_r of 4.0, 5.9 and 8.75 $\mu C/cm^2$ and E_c of 1.65, 1.53 and 1.8 MV/cm respectively correspond well with previous literature on undoped hafnium oxide, where P_r range between 1-10 $\mu C/cm^2$ and E_c between 0.8-2.0 MV/cm [4,33,66]. The results are therefore believed to be reasonable. However, all of the mentioned literature is on undoped ferroelectric hafnia by thermal ALD. To the knowledge of the author and at the time of this publication this is the first time ferroelectricity in undoped hafnia has been achieved with plasma assisted atomic layer deposition.

The P-E curves does not fully have the expected shape, with a down-turn at high fields. This rounding is believed to come from leakage current and needs to be corrected for in order to determine the proper hysteresis curves. In order to combat the leakage current the frequency of the input signal was increased with the motivation, that for a shorter duration at the highest field, the leakage current would decrease.

Since leakage currents can give rise to a hysteresis curve [70] it is crucial to denote that this is not the case. By comparing the V-T graphs in figure 5.13 with previously published literature [8,36] within the subject where ferroelectricity has been observed, the results are strikingly similar (see figure 5.14). A second observation backing this argument is the presence of a small yet noticeable leakage peak occurring at the highest fields in the V-T curves for the samples. This peak is most clearly seen for OPT1:C but present in all the samples. From this it is once again concluded that the large peak does not stem from leakage.

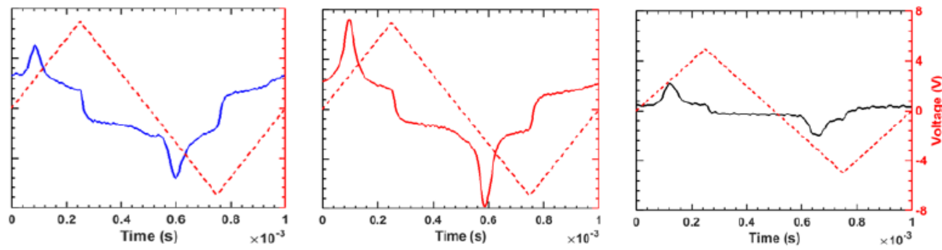

Figure 5.14: I-T curves of ferroelectric oxides by Karine Florent. Image Taken from [8]

From plots of the dielectric constant ϵ_r the variation occurring for different fields is a result of the switching. With ϵ_r reaching a value of up to 30 this indicates that there are more crystal phases present than the monoclinic one. The data from these measurements correspond well with previous J-V results where use of the PF model a dielectric constant of 27 was derived. This seems to be quite accurate having the samples OPT1:A and C reaching an ϵ_r of 25 and 30. Regarding the lower value of 15.4 for OPT1:B it is believed that full switching is not achieved of this device. Yet the same behaviour is observed for ϵ_r just not as pronounced. Nevertheless this device experiences the least leakage currents yielding a more "ideal" P-E curve than the others.

With these results in mind it is relevant to touch up on the fact that in order to more extensively determine the dielectric constant for the thin films C-V measurements need to be conducted. From these the dielectric constant can be derived independently of the P-E curve resulting in a more reliable comparison. Unfortunately there was no time to conduct these measurements during this thesis work.

Chapter 6

Conclusions

With the ability to grow ferroelectric HfO_2 at LNL a new world of possibilities arises. Yet further investigation is necessary to evaluate yield and reproducibility.

In this work plasma assisted ALD grown HfO_2 has been produced and studied with its properties evaluated. Calibration of a new precursor source TEMAHf for the deposition process has been developed. With variation of parameters such as pulse lengths, plasma duration, plasma power, oxygen flow and purge times the leakage current and the breakdown voltage of the films has been vastly improved.

With optimization of the HfO_2 films, (Au/TiN/HfO_2/TiN/Si) MIM structures have been produced. Both optical and electrical characterization of the films has been done with the results presented in chapter 5.

Applying Fowler-Nordheim, Schottky and Poole-Frenkel models the dominating leakage mechanism was determined for the thin films post annealing and as-deposited. The PF model was determined to best fit the measured J-V data.

Furthermore, with the use of the Virtual Ground method, P-E curves have been presented with clear hysteresis. The data have been explained and ferroelectric behaviour of the films was observed. At the time of writing this is, to the knowledge of the author, the first time ever where ferroelectricity in undoped HfO_2 is achieved for a PE-ALD process.

Structures with P_r of 4.0, 5.9 and 8.75 $\mu C/cm^2$ and E_c of 1.65, 1.53 and 1.8 MV/cm respectively were demonstrated. The dielectric constant ϵ_r was measured up to 30.

With the results of this thesis in mind there are fascinating work to be done from here on. Unfortunately the TEMAHf precursor ran out during the work and only one sample with the optimized settings was fabricated.

Future work should involve a sample series with varying thickness and annealing temperature in order to investigate the conditions that optimizes the ferroelectric properties of the films.

A method for leakage current compensation needs to be developed, to remove distortion and acquire good P-E curves. Furthermore, since the application of the films is on transistors where switching occurs millions of times the endurance of the film becomes crucial. It is therefore required to develop a method to determine the films endurance.

Additionally C-V measurements needs to be conducted on the samples to independently of P-E measurements derive the relation between the dielectric constant

and electric field. Moreover the impact of increased argon flow during the HfO_2 deposition should be evaluated, both by itself and with the change in oxygen flow.

Finally GIXRD measurements should be done to evaluate the crystallographic nature of the films and the phases present in them.

The integration of ferroelectric HfO_2 in transistor technology at LNL has a bright future with this work breaking new ground and laying the foundation of further research.

References

[1] J. Valasek, "Piezo-electric and allied phenomena in rochelle salt," *Physical review*, vol. 17, no. 4, p. 475, 1921.

[2] D. Damjanovic, "Hysteresis in piezoelectric and ferroelectric materials," *The science of hysteresis*, vol. 3, pp. 337–465, 2006.

[3] D. Shin, R. Arróyave, and Z.-K. Liu, "Thermodynamic modeling of the hf–si–o system," *Calphad*, vol. 30, no. 4, pp. 375–386, 2006.

[4] P. Polakowski and J. Müller, "Ferroelectricity in undoped hafnium oxide," *Applied Physics Letters*, vol. 106, no. 23, p. 232905, 2015.

[5] T. Böscke, J. Müller, D. Bräuhaus, U. Schröder, and U. Böttger, "Ferroelectricity in hafnium oxide thin films," *Applied Physics Letters*, vol. 99, no. 10, p. 102903, 2011.

[6] S.-L. Hsu, "Hafnium oxide films for application as gate dielectric," 2005.

[7] D. Monsma and J. Becker, "The savannah ald system-an excellent tool for atomic layer deposition," *Material Matters*, vol. 1, no. 3, 2006.

[8] K. Florent, "Ferroelectric hfo2 for emerging ferroelectric semiconductor devices," 2015.

[9] R. G. Arns, "The other transistor: early history of the metal-oxide semiconductor field-effect transistor," *Engineering Science & Education Journal*, vol. 7, no. 5, pp. 233–240, 1998.

[10] A. I. Khan, C. W. Yeung, C. Hu, and S. Salahuddin, "Ferroelectric negative capacitance mosfet: Capacitance tuning & antiferroelectric operation," in *Electron Devices Meeting (IEDM), 2011 IEEE International*. IEEE, 2011, pp. 11–3.

[11] D. Kwon, K. Chatterjee, A. J. Tan, A. K. Yadav, H. Zhou, A. B. Sachid, R. Dos Reis, C. Hu, and S. Salahuddin, "Improved subthreshold swing and short channel effect in fdsoi n-channel negative capacitance field effect transistors," *IEEE Electron Device Letters*, vol. 39, no. 2, pp. 300–303, 2018.

[12] B. G. S. B. Streetman, "Solid state electronic devices," *New Jersey: Prentice Hall*, vol. 5th ed, p. 524, 2000.

[13] S. Sze and M. Lee, "Semiconductor devices: Physics and technology," *John Wiley Sons*, vol. 3rd ed, 2013.

[14] S. Salahuddin and S. Datta, "Use of negative capacitance to provide voltage amplification for low power nanoscale devices," *Nano letters*, vol. 8, no. 2, pp. 405–410, 2008.

[15] K.-S. Li, P.-G. Chen, T.-Y. Lai, C.-H. Lin, C.-C. Cheng, C.-C. Chen, Y.-J. Wei, Y.-F. Hou, M.-H. Liao, M.-H. Lee *et al.*, "Sub-60mv-swing negative-capacitance finfet without hysteresis," in *Electron Devices Meeting (IEDM), 2015 IEEE International*. IEEE, 2015, pp. 22–6.

[16] W. Känzig, "Ferroelectrics and antiferroeletrics," in *Solid State Physics*. Elsevier, 1957, vol. 4, pp. 1–197.

[17] A. Luker, "A short history of ferroelectricity," *Instituto Superior Técnico Departamento de Física*.

[18] C. H. A. K. Rabe and J.-M., "Physics of ferroelectrics: A modern perspective," *Triscone*, 2007.

[19] C.-K. Lee, E. Cho, H.-S. Lee, C. S. Hwang, and S. Han, "First-principles study on doping and phase stability of hfo_2," *Phys. Rev. B*, vol. 78, p. 012102, Jul 2008. [Online]. Available: https://link.aps.org/doi/10.1103/PhysRevB.78.012102

[20] D. Fischer and A. Kersch, "The effect of dopants on the dielectric constant of hf o 2 and zr o 2 from first principles," *Applied Physics Letters*, vol. 92, no. 1, p. 012908, 2008.

[21] K. Kukli, J. Aarik, M. Ritala, T. Uustare, T. Sajavaara, J. Lu, J. Sundqvist, A. Aidla, L. Pung, A. Hårsta *et al.*, "Effect of selected atomic layer deposition parameters on the structure and dielectric properties of hafnium oxide films," *Journal of applied physics*, vol. 96, no. 9, pp. 5298–5307, 2004.

[22] N. Nikolaou, P. Dimitrakis, P. Normand, V. Ioannou-Sougleridis, K. Giannakopoulos, K. Mergia, K. Kukli, J. Niinistö, M. Ritala, and M. Leskelä, "Influence of atomic layer deposition chemistry on high-k dielectrics for charge trapping memories," *Solid-State Electronics*, vol. 68, pp. 38–47, 2012.

[23] M.-Y. Ho, H. Gong, G. Wilk, B. Busch, M. Green, P. Voyles, D. Muller, M. Bude, W. Lin, A. See *et al.*, "Morphology and crystallization kinetics in hfo 2 thin films grown by atomic layer deposition," *Journal of Applied Physics*, vol. 93, no. 3, pp. 1477–1481, 2003.

[24] S. Ushakov, A. Navrotsky, Y. Yang, S. Stemmer, K. Kukli, M. Ritala, M. Leskelä, P. Fejes, A. Demkov, C. Wang *et al.*, "Crystallization in hafnia- and zirconia-based systems," *physica status solidi (b)*, vol. 241, no. 10, pp. 2268–2278, 2004.

[25] O. Ohtaka, H. Fukui, T. Kunisada, T. Fujisawa, K. Funakoshi, W. Utsumi, T. Irifune, K. Kuroda, and T. Kikegawa, "Phase relations and equations of state of zro 2 under high temperature and high pressure," *Physical Review B*, vol. 63, no. 17, p. 174108, 2001.

[26] X. Zhao and D. Vanderbilt, "First-principles study of electronic and dielectric properties of zro 2 and hfo 2," *MRS Online Proceedings Library Archive*, vol. 747, 2002.

[27] T. Böscke, P. Hung, P. Kirsch, M. Quevedo-Lopez, and R. Ramírez-Bon, "Increasing permittivity in hfzro thin films by surface manipulation," *Applied Physics Letters*, vol. 95, no. 5, p. 052904, 2009.

[28] S. Mueller, J. Mueller, A. Singh, S. Riedel, J. Sundqvist, U. Schroeder, and T. Mikolajick, "Incipient ferroelectricity in al-doped hfo2 thin films," *Advanced Functional Materials*, vol. 22, no. 11, pp. 2412–2417, 2012.

[29] J. Müller, U. Schröder, T. Böscke, I. Müller, U. Böttger, L. Wilde, J. Sundqvist, M. Lemberger, P. Kücher, T. Mikolajick *et al.*, "Ferroelectricity in yttrium-doped hafnium oxide," *Journal of Applied Physics*, vol. 110, no. 11, p. 114113, 2011.

[30] U. Schroeder, C. Richter, M. H. Park, T. Schenk, M. Pesic, M. Hoffmann, F. P. Fengler, D. Pohl, B. Rellinghaus, C. Zhou *et al.*, "Lanthanum-doped hafnium oxide: A robust ferroelectric material," *Inorganic chemistry*, vol. 57, no. 5, pp. 2752–2765, 2018.

[31] M. Kozodaev, A. Chernikova, E. Korostylev, M. Park, U. Schroeder, C. Hwang, and A. Markeev, "Ferroelectric properties of lightly doped la: Hfo2 thin films grown by plasma-assisted atomic layer deposition," *Applied Physics Letters*, vol. 111, no. 13, p. 132903, 2017.

[32] J. Müller, P. Polakowski, S. Mueller, and T. Mikolajick, "Ferroelectric hafnium oxide based materials and devices: Assessment of current status and future prospects," *ECS Journal of Solid State Science and Technology*, vol. 4, no. 5, pp. N30–N35, 2015.

[33] A. Pal, V. K. Narasimhan, S. Weeks, K. Littau, D. Pramanik, and T. Chiang, "Enhancing ferroelectricity in dopant-free hafnium oxide," *Applied Physics Letters*, vol. 110, no. 2, p. 022903, 2017.

[34] D. Triyoso, P. Tobin, B. White Jr, R. Gregory, and X. Wang, "Impact of film properties of atomic layer deposited hf o 2 resulting from annealing with a tin capping layer," *Applied physics letters*, vol. 89, no. 13, p. 132903, 2006.

[35] T. Böscke, S. Teichert, D. Bräuhaus, J. Müller, U. Schröder, U. Böttger, and T. Mikolajick, "Phase transitions in ferroelectric silicon doped hafnium oxide," *Applied Physics Letters*, vol. 99, no. 11, p. 112904, 2011.

[36] M. H. Park, Y. H. Lee, H. J. Kim, Y. J. Kim, T. Moon, K. D. Kim, J. Mueller, A. Kersch, U. Schroeder, T. Mikolajick *et al.*, "Ferroelectricity and antiferroelectricity of doped thin hfo2-based films," *Advanced Materials*, vol. 27, no. 11, pp. 1811–1831, 2015.

[37] A. I. Khan, K. Chatterjee, B. Wang, S. Drapcho, L. You, C. Serrao, S. R. Bakaul, R. Ramesh, and S. Salahuddin, "Negative capacitance in a ferroelectric capacitor," *Nature materials*, vol. 14, no. 2, p. 182, 2015.

[38] V. V. Zhirnov and R. K. Cavin, “Nanoelectronics: Negative capacitance to the rescue?” *Nature Nanotechnology*, vol. 3, no. 2, p. 77, 2008.

[39] J. C. Ranuárez, M. J. Deen, and C.-H. Chen, “A review of gate tunneling current in mos devices,” *Microelectronics reliability*, vol. 46, no. 12, pp. 1939–1956, 2006.

[40] H. Chen, F. Chiu, C.-H. Liu, S. Chen, H. Huang, P. Juan, and H. Hwang, “Interface characterization and current conduction in hfo2-gated mos capacitors,” *Applied Surface Science*, vol. 254, no. 19, pp. 6112–6115, 2008.

[41] R. Entner, “Modeling and simulation of negative bias temperature instability,” 2007.

[42] E. Winqvist, “Leakage current and breakdown of hfo2/ingaas mos capacitors,” 2015.

[43] M. Lenzlinger and E. Snow, “Fowler-nordheim tunneling into thermally grown sio2,” *Journal of Applied physics*, vol. 40, no. 1, pp. 278–283, 1969.

[44] K. Y. Cheong, J. H. Moon, H. J. Kim, W. Bahng, and N.-K. Kim, “Current conduction mechanisms in atomic-layer-deposited hfo 2/nitrided sio 2 stacked gate on 4h silicon carbide,” *Journal of Applied Physics*, vol. 103, no. 8, p. 084113, 2008.

[45] G. Bersuker, J. Yum, L. Vandelli, A. Padovani, L. Larcher, V. Iglesias, M. Porti, M. Nafría, K. McKenna, A. Shluger *et al.*, “Grain boundary-driven leakage path formation in hfo2 dielectrics,” *Solid-State Electronics*, vol. 65, pp. 146–150, 2011.

[46] O. Pirrotta, L. Larcher, M. Lanza, A. Padovani, M. Porti, M. Nafría, and G. Bersuker, “Leakage current through the poly-crystalline hfo2: Trap densities at grains and grain boundaries,” *Journal of Applied Physics*, vol. 114, no. 13, p. 134503, 2013.

[47] T. Lee and S. K. Banerjee, “Reduced gate-leakage current and charge trapping characteristics of dysprosium-incorporated hfo_2 gate-oxide n-mos devices,” *IEEE Transactions on Electron Devices*, vol. 58, no. 2, pp. 562–566, 2011.

[48] A. Toriumi and H. Satake, “The boundary between hard-and soft-breakdown in ultrathin silicon dioxide films,” *MRS Online Proceedings Library Archive*, vol. 592, 1999.

[49] S. M. Sze, *Semiconductor devices: physics and technology.* John Wiley & Sons, 2008.

[50] M. Ritala and M. Leskelä, “Atomic layer deposition,” in *Handbook of Thin Films.* Elsevier, 2002, pp. 103–159.

[51] D.-H. Kim, D.-H. Kim, H.-I. Seo, and Y.-C. Kim, “Interaction of temahf precursor with oh-terminated si (001) surface: a first principles study,” *Journal of nanoscience and nanotechnology*, vol. 11, no. 5, pp. 4324–4327, 2011.

[52] X. Liu, S. Ramanathan, A. Longdergan, A. Srivastava, E. Lee, T. E. Seidel, J. T. Barton, D. Pang, and R. G. Gordon, "Ald of hafnium oxide thin films from tetrakis (ethylmethylamino) hafnium and ozone," *Journal of the electrochemical society*, vol. 152, no. 3, pp. G213–G219, 2005.

[53] H. Kim and I.-K. Oh, "Review of plasma-enhanced atomic layer deposition: Technical enabler of nanoscale device fabrication," *Japanese Journal of Applied Physics*, vol. 53, no. 3S2, p. 03DA01, 2014.

[54] F. L. McCrackin, E. Passaglia, R. R. Stromberg, and H. L. Steinberg, "Measurement of the thickness and refractive index of very thin films and the optical properties of surfaces by ellipsometry," *J. Res. Nat. Bur. Sec. A*, vol. 67, 1963.

[55] K.-J. E. Karsten Hinrichs, "Ellipsometry of functional organic surfaces and films," p. Chap. Ellipsometry: A Survey of Concept, 2018.

[56] H. Tompkins and E. A. Irene, *Handbook of ellipsometry.* William Andrew, 2005.

[57] J. Woollam. Ellipsometry tutorial. [Online]. Available: https://www.jawoollam.com/resources/ellipsometry-tutorial

[58] G. Binnig, C. F. Quate, and C. Gerber, "Atomic force microscope," *Physical review letters*, vol. 56, no. 9, p. 930, 1986.

[59] E. Meyer, "Atomic force microscopy," *Progress in surface science*, vol. 41, no. 1, pp. 3–49, 1992.

[60] S. Kalpakjian, K. Vijai Sekar, and S. R. Schmid, *Manufacturing engineering and technology.* Pearson, 2014.

[61] L. Bartholomew, C. Barelli, J. Owyang, R. DiCarlo, D. Shenai, C. Marsman, and Y. Senzaki, "Comparison of ald of hfo2, sio2, and hfsiox thin films using various metal/silicon alkylamide precursors and o3," *ECS Transactions*, vol. 3, no. 15, pp. 37–49, 2007.

[62] D. M. Hausmann, E. Kim, J. Becker, and R. G. Gordon, "Atomic layer deposition of hafnium and zirconium oxides using metal amide precursors," *Chemistry of materials*, vol. 14, no. 10, pp. 4350–4358, 2002.

[63] D. Hall, M. Cain, M. Stewart, T. U. K. C. f. M. M. National Physical Lab., and Technology;, "Ferroelectric hysteresis measurement & analysis," in *Minutes of the NPL CAM7 IAG Meeting*, 1998.

[64] K. Kukli, M. Ritala, M. Leskelä, T. Sajavaara, J. Keinonen, A. C. Jones, and J. L. Roberts, "Atomic layer deposition of hafnium dioxide films using hafnium bis (2-butanolate) bis (1-methoxy-2-methyl-2-propanolate) and water," *Chemical Vapor Deposition*, vol. 9, no. 6, pp. 315–320, 2003.

[65] A. Sharma, V. Longo, M. A. Verheijen, A. A. Bol, and W. Kessels, "Atomic layer deposition of hfo2 using hfcp (nme2) 3 and o2 plasma," *Journal of Vacuum Science & Technology A: Vacuum, Surfaces, and Films*, vol. 35, no. 1, p. 01B130, 2017.

[66] K. Kim, M. Park, H. Kim, Y. Kim, T. Moon, Y. Lee, S. Hyun, T. Gwon, and C. Hwang, "Ferroelectricity in undoped-hfo 2 thin films induced by deposition temperature control during atomic layer deposition," *Journal of Materials Chemistry C*, vol. 4, no. 28, pp. 6864–6872, 2016.

[67] S. Starschich, S. Menzel, and U. Böttger, "Evidence for oxygen vacancies movement during wake-up in ferroelectric hafnium oxide," *Applied Physics Letters*, vol. 108, no. 3, p. 032903, 2016.

[68] T. Gupta, "Dielectric materials," in *Copper Interconnect Technology*. Springer, 2009, pp. 67–110.

[69] R. Pandey, R. Sathiyanarayanan, U. Kwon, V. Narayanan, and K. Murali, "Role of point defects and hfo2/tin interface stoichiometry on effective work function modulation in ultra-scaled complementary metal–oxide–semiconductor devices," *Journal of Applied Physics*, vol. 114, no. 3, p. 034505, 2013.

[70] J. Scott, "Ferroelectrics go bananas," *Journal of Physics: Condensed Matter*, vol. 20, no. 2, p. 021001, 2007.

Appendix A

MATLAB Code For P-E Curves

```
1    %clc, clear all,clf;
2 -  data = readOscilloscope('WA000020.CSV');
3 -  dt = data(2,1)-data(1,1);
4 -  e0 =8.85419e-12;
5 -  tid =3e-6;
6 -  r = 25e-4 %/cm;
7 -  A = pi*r^2;
8 -  sensitivity = 5*10^-6;
9 -  d = 10e-7 %/cm;
10 - x = -round(tid/dt);
11 - grader= x/3200*360
12
13
14 - v_E = data(800+x:8000+x,2);
15 - v_P = data(800:8000,3);
16
17 - i = v_P.*sensitivity;
18 - E = 1e-6.*v_E./d;
19
20 - Q(1) = max(i)*dt;
21 - for t = 2:length(v_E)
22 -     Q(t) = i(t)*dt+Q(t-1);
23 - end
24
25 - P = (Q./A)*1e6;
26 - maxvalue = max(P);
27 - minvalue = min(P);
28 - difference = (maxvalue - minvalue)/2;
29 - correction = abs(difference + minvalue);
30 - P = P-abs(correction);
31   %subplot(3,3,8);
32
33   %er = abs(transpose(P)./(1e6*e0.*abs(E)));
34 - plot(E,P,'k','Linewidth',1.5)
35 - ax = gca;
36 - ax.XAxisLocation = 'origin';
37 - ax.YAxisLocation = 'origin';
38 - ylim([-15 15])
39   %set(gca, 'YTick', [])
40 - title('P-E Curve of Optimized Sample')
41 - xlabel('Electric Field [MV/cm]')
42 - ylabel('Polarization [\muC/cm^2]')
43   %subplot(3,3,7)
44 - figure
45 - plot(data(800:8000,1).*1e6,v_E)
46 - hold on
```

Figure A.1: MATALB code for P-E curves.

```
47 -    plot(data(800:8000,1).*1e6,v_P)
48 -    ylabel('Voltage [V]')
49 -    xlim([-150 150])
50 -    ylim([-6 6])
51 -    title('V-T Curve of Optimized Sample')
52 -    xlabel('Time [\mus]')
53 -    ylabel('Voltage [V]')
54 -    set(gca,'FontSize',18)
55      % Create second Y axes on the right.
56      % a2 = axes('YAxisLocation', 'Right')
57      % Hide second plot.
58      % set(a2, 'color', 'none')
59      % set(a2, 'XTick', [])
60      % Set scala for second Y.
61      % set(a2, 'YLim', [-3 4])
62      % ylabel('Electric Field [MV/cm]')
63 -    hold off
64      %%
65 -    plot(data(800:8000),i)
66 -    hold on
67 -    yyaxis right
68 -    plot(data(800:8000),v_E)
69 -    figure
70 -    plot(E,i)
71      %%
72 -    sens = 1e-6;
73 -    Area =21e-6^2*pi;
74 -    d = 1e-8;
75 -    dvdt = 1.5e5;
76 -    maximum = max(v_E);
77 -    minimum = min(v_E);
78 -    first = find(v_E==maximum);
79 -    second = find(v_E==minimum);
80 -    dv = (v_E(first(1))-(v_E(second(1))));
81 -    dt1 = (data(first(1),1)-data(second(1),1));
82 -    dvdt1 = dv/dt1;
83 -    start=1;
84 -    e = 3500;
85 -    C = (v_P(start:e).*sens)./dvdt1;
86 -    e_r = (C.*d)./(Area*e0);
87 -    plot(E(start:e),abs(e_r),'k*')
88 -    ylim([0 35])
89 -    title('Dielectric Constant vs Electric Field for Optimized Sample')
90 -    xlabel('Electric Field [MV/cm]')
91 -    ylabel('Dielectric constant \epsilon_r')
```

Figure A.2: MATALB code for P-E curves.

```
1       function [dataArray] = readOscilloscope(filename)
2
3 -         startRow = 11; % The oscilloscope has text variables in the first rows
4 -         formatSpec = '%f%f%f%*s%*s%[^\n\r]'; % Format for each line of text: For more information, see the TEXTSCAN documentation.
5
6 -         fileID = fopen(filename,'r');
7 -         dataArray = textscan(fileID, formatSpec, 'Delimiter', ',', 'MultipleDelimsAsOne', true, 'TextType', 'string'...
8           ,'EmptyValue', NaN, 'HeaderLines' ,startRow-1, 'ReturnOnError', false, 'EndOfLine', '\r\n');
9 -         fclose(fileID);
10 -        dataArray = [dataArray{1:end-1}];
11
12
13 -     end
```

Figure A.3: MATLAB code to read input data from measurements.

Appendix B

Old Recipe HfO2

In figure B.1 the standard recipe provided with the Fiji F200 ALD is shown. Available at `www.nanolab.ucla.edu/pdf/ALD_Fiji.pdf`.

Standard Plasma HfO_2 Recipe at 200°C

	Instruction	#	Value	
0	flow	0	20	Set precursor manifold stand-by Ar flow rate
1	flow	1	40	Set plasma source stand-by Ar flow rate
2	heater	12	**200**	Set trap/cone temperature
3	heater	13	**200**	Set reactor zone 1 temperature
4	heater	14	**200**	Set reactor zone 2 temperature
5	heater	15	**200**	Set chuck temperature
6	heater	16	150	Set precursor delivery line to 150°C
7	heater	17	150	Set precursor manifold to 150°C
8	Heater	19	75	Set precursor bottle to 75°C
9	stabilize	12		Wait for trap/cone temperature to stabilize
10	stabilize	13		Wait for reactor zone 1 temperature to stabilize
11	stabilize	14		Wait for reactor zone 2 temperature to stabilize
12	stabilize	15		Wait for chuck temperature to stabilize
13	stabilize	19		Wait for precursor bottle to stabilize
14	wait		600	Wait for substrate temperature to stabilize
15	MFCvalve	3	1	Set precursor manifold Ar for expo step
16	flow	0	60	
17	flow	1	200	
18	APC		**9**	Set throttle valve
19	wait		20	Wait for Ar MFCs to stabilize
20	pulse	2	0.25	Begin loop. Pulse Hf. Hf = Hf ALD Valve number
21	wait		**5**	Purge Hf and reaction by-products
22	flow	3	20	Start O_2 flow
23	wait		5	
24	plasma		300	Turn on plasma.
25	wait		20	
26	plasma	0	0	Turn off plasma.
27	flow	3	0	Start O_2 flow.
28	wait		**5**	Purge O_2 and reaction by-products
29	**goto**	**19**	**X**	**Input # of cycles, number, x = cycles, GPC ~ 1A/cycle**
30	flow	0	5	
31	flow	1	10	
32	flow	3	0	Turn off O_2
33	APC		100	Open throttle valve. If no throttle valve, remove this line
34	turbopurge		0	
35	doorpurge		0	

Figure B.1: Standard recipe for HfO_2 at 200°C.